Energy & Environmental Science

ROYAL SOCIETY OF CHEMISTRY

REVIEW

View Article Online
View Journal | View Issue

Cite this: *Energy Environ. Sci.*, 2021, **14**, 1771

Passive, high-efficiency thermally-localized solar desalination

Lenan Zhang,[a] Zhenyuan Xu,†[ab] Lin Zhao,†[a] Bikram Bhatia,†[c] Yang Zhong,[a] Shuai Gong[a] and Evelyn N. Wang*[a]

Received 22nd December 2020,
Accepted 16th March 2021

DOI: 10.1039/d0ee03991h

rsc.li/ees

Solar desalination holds significant promise for the water-energy nexus. Recent advances in passive solar desalination using thermal localization show great potential for high-efficiency freshwater production, which is particularly beneficial for areas without well-established water and energy infrastructure. However, there is a significant knowledge gap between laboratory scale innovation and commercial adoption. In this review, we discuss two critical factors – water production and reliability – which, if addressed systematically, could enable high-performance thermally-localized solar desalination systems. We show that optimizing heat and mass transfer of the entire device and recycling the latent heat of condensation are important to enhance total water production. Meanwhile, we discuss the potential of novel system architectures and fluid flow engineering to enable anti-fouling and robust desalination devices. In addition, we present techno-economic analysis that highlights the balance between water production, reliability, and cost. A criterion for economic feasibility is provided by comparing the price of desalinated water with commercially available bottle and tap water, which provides a roadmap for future development of solar desalination technologies.

Broader context

More than one half of the global population is experiencing water scarcity. Desalinating seawater using natural sunlight takes advantage of two abundant resources, and could provide a sustainable solution to water shortage. However, conventional solar desalination systems either require well-established infrastructure or suffer from low energy efficiency, which has thus far limited their widespread adoption. The recent development of thermally-localized solar desalination enables passive and high-efficiency water production, providing a promising approach to address water shortages in underdeveloped regions. Although tremendous efforts have led to significant innovations in materials and evaporator designs for thermally-localized solar desalination, a device-level perspective considering both water production and reliability is limited, which is crucial for commercially competitive water production. In this review, we discuss the recent progress of thermally-localized solar desalination, with a focus on operating configurations, optimizing water production, and enhancing anti-fouling property. This article also provides a perspective on future opportunities, which could enable next-generation solar desalination technologies.

1. Introduction

During the last few decades, it has become evident that freshwater scarcity is becoming a threat to sustainable development of human society due to a steadily increasing demand.[1,2] In its most recent annual risk report, the World Economic Forum listed water crises as the largest global risk in terms of potential impact.[3] The increasing world population, improving living standards, changing consumption patterns, and expansion of irrigated agriculture are the main driving forces for the rising global demand for water. As a consequence, a significant fraction of the world population faces water scarcity (Fig. 1a) – 17 countries classified as extremely high water stressed and another 27 high stressed countries, particularly concentrated around the Middle East, North Africa and Sub-Saharan Africa. Several of these countries are also resource-constrained and cannot afford expensive large-scale energy-intensive desalination technologies to meet their freshwater needs.[4,5] Fortunately, many of the water-stressed countries have access to ample solar radiation resource which can enable low-cost distributed renewable water desalination technologies.[6]

Solar thermal desalination offers a path towards low-cost, modular and high-efficiency desalination systems that are

[a] *Department of Mechanical Engineering, Massachusetts Institute of Technology, Cambridge, MA 02139, USA. E-mail: enwang@mit.edu*
[b] *Institute of Refrigeration and Cryogenics, Shanghai Jiao Tong University, Shanghai 200240, China*
[c] *Department of Mechanical Engineering, University of Louisville, Louisville, KY 40292, USA*
† Equal contribution to this work.

powered by renewable energy and are ideally suited for resource-constrained environments.[7–9] Solar thermal desalination relies on the conversion of solar radiation to heat, which is then used for vapor generation, and consequently condensed to produce clean water. These systems can be passive, portable and economical because they can be fabricated with readily available low-cost materials and do not require electricity. While reverse osmosis is the dominant technology for large-scale systems, thermal desalination systems offer a modular approach that can fulfill the water needs of a household.[2,7]

Significant research has focused on improving the performance of solar thermal desalination systems. Specifically, the focus has been to maximize the solar-to-vapor conversion efficiency, defined as,[8–11]

$$\eta = \frac{\dot{m} h_{fg}}{A q''_{sun}} \quad (1)$$

where $\dot{m}$ is the evaporation rate, h_{fg} is the latent heat of vaporization, A is the area of solar absorber, and q''_{sun} is the incident solar flux. The solar-to-vapor conversion efficiency accounts for the effectiveness of solar-thermal energy conversion, the rate of thermal energy conversion used for evaporation, and the degree to which the latent heat of condensation is reused for further distillation (often quantified as the gain output ratio, GOR).[7,12] Another key metric that incorporates both the solar-to-vapor and vapor-to-water generation processes is the water production rate, which quantifies the water produced per unit absorber area per unit time (units: L m^{-2} h^{-1}).[7–14] However, water production rate of a desalination device depends on the incident solar flux. To quantify the intrinsic capability of water production, the water productivity is also commonly used, which is defined as the ratio of water production rate to incident solar flux (units: L kWh^{-1}) and scaled with η by the proportional constant h_{fg}.[15]

Solar desalination technologies span a wide range of complexity and performance levels – depicted in Fig. 1b. Solar still – the earliest and most basic solar desalination technology is simple, cheap and passive.[16] However, the operational and theoretical efficiencies are typically less than 45%[10,17,18] and

Lenan Zhang

Lenan Zhang is a PhD candidate in the Department of Mechanical Engineering at the Massachusetts Institute of Technology. He received his dual BS from Shanghai Jiao Tong University and Purdue University, and MS from the Massachusetts Institute of Technology in Mechanical Engineering. His research interests include fundamental studies of micro/nanoscale transport processes, metrology, and their applications in thermal management and solar thermal systems.

Zhenyuan Xu

Zhenyuan Xu is an Associate Professor in the School of Mechanical Engineering at Shanghai Jiao Tong University (SJTU). He received his BS in 2010, and PhD in Power Engineering and Engineering Thermophysics from SJTU in 2015, respectively. Prior to joining SJTU, he was a postdoc fellow at the Massachusetts Institute of Technology. His research interests include the utilization of solar energy and waste heat in desalination, sorption heat pump and sorption heat storage.

Lin Zhao

Lin Zhao is a Thin Film Optics Design Engineer at 3M. He received his BS in Physics and Mathematics from Tsinghua University in 2012, his MS in Nanotechnology from the University of Pennsylvania in 2014, and his PhD in Mechanical Engineering from the Massachusetts Institute of Technology in 2019. His research interests include heat transfer, optics, and novel materials for energy systems.

Bikram Bhatia

Bikram Bhatia is an Assistant Professor in the Department of Mechanical Engineering at the University of Louisville (UofL). Prior to joining UofL in 2019, he was a research scientist at the Massachusetts Institute of Technology. Bikram received his BTech from the Indian Institute of Technology Guwahati in 2008, and PhD in mechanical engineering from the University of Illinois at Urbana-Champaign in 2014. His research interests include heat transfer, nanotechnology, advanced materials, and energy systems.

70%,[19,20] respectively, due to the poor thermal management and loss of vaporization enthalpy. Slightly more complex multi-stage or multi-effect solar stills with condensation heat recovery enable improved performance. These multi-stage devices achieve operational and theoretical efficiencies up to 90%[21] and 160%,[22] respectively, while maintaining passive operation. Despite passive operation and low cost of solar stills, their low efficiency and productivity make the produced water expensive. To achieve high-efficiency solar desalination, passive operability is sacrificed to improve heat and mass transfer – implemented in active solar stills and solar humidification-dehumidification systems that are typically powered by solar collectors and photovoltaics. The active control of heat and mass transport pushes the operational and theoretical efficiencies to 320%[23] and 650%,[24] respectively. Even greater performance enhancement can be achieved by large-scale multi-effect distillation and multi-stage flash systems, which can reach operational and ideal efficiencies up to 1100%[25] and 5000%,[16] respectively. However, these systems require a vacuum and significant power resources – possible only in centralized solar desalination facilities. Thus, there exists a clear trade-off between flexibility and performance of conventional solar desalination technologies.

Recent developments, particularly those relying on thermal localization[26–33] and latent heat reutilization,[15,34,35] have demonstrated the potential for high-performance, passive, and portable solar desalination, which enables the simultaneous improvement of flexibility and efficiency (yellow-shaded area in Fig. 1b). Experimentally demonstrated efficiency as high as 385% – comparable to that of active solar desalination systems – have already been demonstrated.[34] With design optimization, even higher efficiencies – as high as 750% – could be possible.[36] However, while these significant advances in performance have been realized through the development of novel materials and configurations for solar thermal desalination, a quantitative understanding of heat and mass transport that has enabled these performance enhancements is lacking. In addition, the vast majority of reported studies have focused on vapor generation, while the other half of the desalination process – efficient condensation and effective recovery of the latent heat of condensation have received relatively less attention. Therefore, a systematic framework is needed that evaluates performance contribution of each process and helps identify the most effective strategies to achieve high-performance solar thermal desalination. Such a framework is also necessary to compare the performance of devices with different designs, tested under varied experimental conditions. Furthermore, practical challenges such as fouling due to salt accumulation that affect the reliability need to be addressed. We believe, a quantitative understanding of transport within each component of a solar desalination system will help identify the key bottlenecks and provide design solutions to maximize performance, improve reliability, and reduce cost.

The goal of this paper is to analyze past works on thermally-localized solar desalination, identify critical gaps in knowledge, and use a quantitative approach to determine areas that could improve performance. Specifically, we focus on the following key aspects. (1) Develop a general framework to identify different configurations, heat loss mechanisms, fundamental limits of performance, and bottlenecks for evaporator design. (2) Evaluate heat and mass transport within different configurations of high-performance solar desalination devices based on thermal localization, and provide a roadmap from the current demonstrated device-level performance to efficiencies and water production rates achievable in the future. (3) Examine salt accumulation in desalination devices and its effect on device performance, and recommend design strategies to balance water production and reliability. (4) Analyze the economics of passive solar-driven desalination systems, and determine the key metrics required to ensure scalability and cost-competitiveness. Addressing the above elements could help realize the full

Yang Zhong

Yang Zhong is a PhD candidate in the Department of Mechanical Engineering at the Massachusetts Institute of Technology. He received his dual BS in Mechanical Engineering from Shanghai Jiao Tong University and Purdue University. Under the supervision of Professor Evelyn N. Wang, his research is focused on energy transport and conversion, with applications to water harvesting and thermal management.

Evelyn N. Wang

Evelyn N. Wang is the Gail E. Kendall Professor and Department Head in the Mechanical Engineering Department at MIT. She received her BS from MIT, and MS and PhD from Stanford University in Mechanical Engineering. Her research interests include fundamental studies of micro/nanoscale heat and mass transport and the development of efficient thermal management, solar thermal energy conversion, and water harvesting and desalination systems. Her work has been honored with awards including the 2012 ASME Bergles-Rohsenow Young Investigator Award, the 2016 ASME EPPD Women Engineer Award, and the 2017 ASME Gustus L. Larson Award. She is an ASME Fellow.

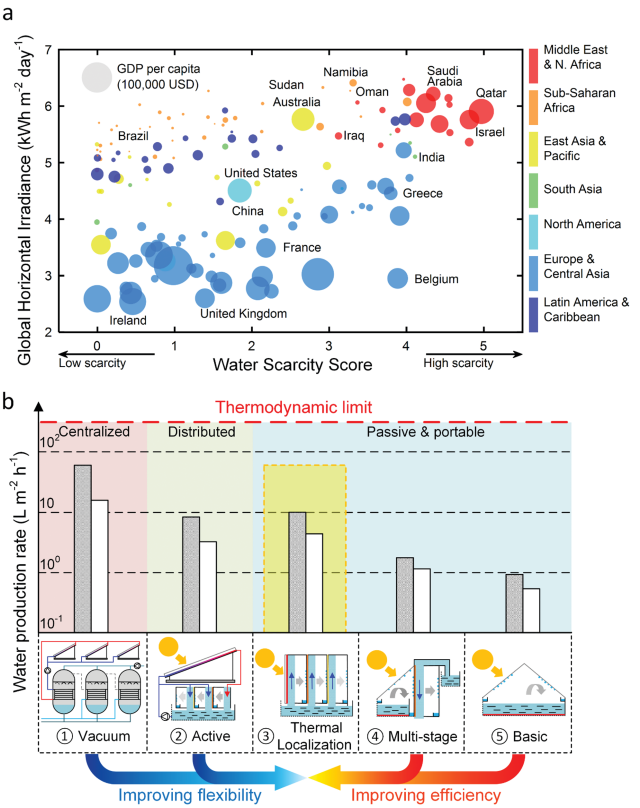

Fig. 1 Water and solar resource distribution in the world, and comparison of desalination technologies. (a) Plot showing the availability of water,[3] average daily solar irradiation,[6] and per capita gross domestic product (GDP) of countries belonging to different regions of the world.[5] Solar thermal desalination offers a promising solution for low-income water-scarce countries with high solar resource availability (smaller circles in the upper-right corner), particularly in the Middle East, North Africa and Sub-Saharan Africa. (b) Water production rate achieved by different solar thermal desalination technologies. The red dashed line represents the thermodynamic limit of solar thermal desalination, and the white and gray bars represent the operational[10,17,18,21,23,25,34] and theoretical[16,19,20,22,24,36] water production rates, respectively.

potential of passive solar desalination and provide a sustainable pathway to meet our freshwater needs.

2. Design of a high-performance evaporator for solar desalination systems

The evaporator constitutes a key component in a solar thermal desalination device that transforms input thermal energy into water vapor. Conventional evaporators are typically comprised of designs where the absorber is far from the evaporating surface.[16–25] In contrast, recent works have focused on evaporator designs that localize the solar-thermal conversion process that reduces heat loss and therefore improves the solar-vapor conversion efficiency.[7,8,10,13] In this section, we review the recent progress in the design of thermally-localized evaporator enabled by material-level innovations and optimized thermal management. In addition to presenting different evaporator configurations and materials, we quantitatively analyze the heat and mass transport characteristics and associated bottlenecks that have received relatively less attention. We provide a general modeling framework for the heat and mass transport which could guide the design of the evaporator and optimization of the vapor generation process.

2.1. Evaporator configurations using thermal localization

In this article, unlike previous reviews that typically categorized evaporator designs based on their material composition and morphology,[8–10,13,14,37–43] we focus on analyzing recent high-efficiency evaporator designs based on their operating configurations. We classify different evaporator configurations based on the relative orientation of the evaporation and the solar absorption processes. In most common evaporators, classified as "front-side" evaporators, the two processes occur on the same side (Fig. 2a). More recently, few works have demonstrated "back-side" evaporator configurations where evaporation occurs on the opposite side of the solar absorber (Fig. 2b).

In front-side designs, the evaporator achieves four main functionalities: (1) solar absorption and conversion to heat, (2) evaporation *via* localized heating, (3) supply water passively using capillary pressure to enable continuous evaporation, and (4) thermally insulate bulk water. To efficiently capture sunlight, a broadband solar absorber is ideal and can be realized using carbonaceous materials,[26,44–52] plasmonic structures,[29,30,53–57] and polymeric materials[31–33,58,59] as shown in Fig. 2c. To enable localized heating, efficient water transport, and thermal insulation, front-side evaporators often comprise porous materials with connected pores to allow a continuous water path. For example, the carbon foam developed by Ghasemi *et al.*[26] and the hierarchical gel developed by Zhao *et al.*[31] have a randomly connected porous structure to achieve interfacial heating, capillary pumping, and heat loss suppression. To further optimize water transport, directional water pathways have also been investigated in natural wood,[49] anodic aluminum oxide (AAO),[29] and three-dimensional structures.[60–62] A fundamentally different front-side design is the contactless configuration,[63,64] where a solar absorber converts sunlight into infrared (IR) thermal radiation. As water is a strong IR absorber, with a penetration depth ~10 μm in IR, most of the thermal radiation is absorbed within a thin water layer – enabling interfacial heating. As the water body itself serves as the absorber and evaporator, external water supply is no longer needed. One drawback of the current contactless evaporator designs is the lack of thermal insulation which results in significant heat loss through the bulk water body.

Several recent studies have optimized front-side evaporators and achieved exceptionally high solar-to-vapor conversion efficiency.[7,10,26,31] However, there are a few inherent limitations associated with front-side design. Firstly, because front-side evaporators combine four functionalities, it poses stringent material property requirements that are difficult to meet. Moreover, vapor collection and condensation are challenging

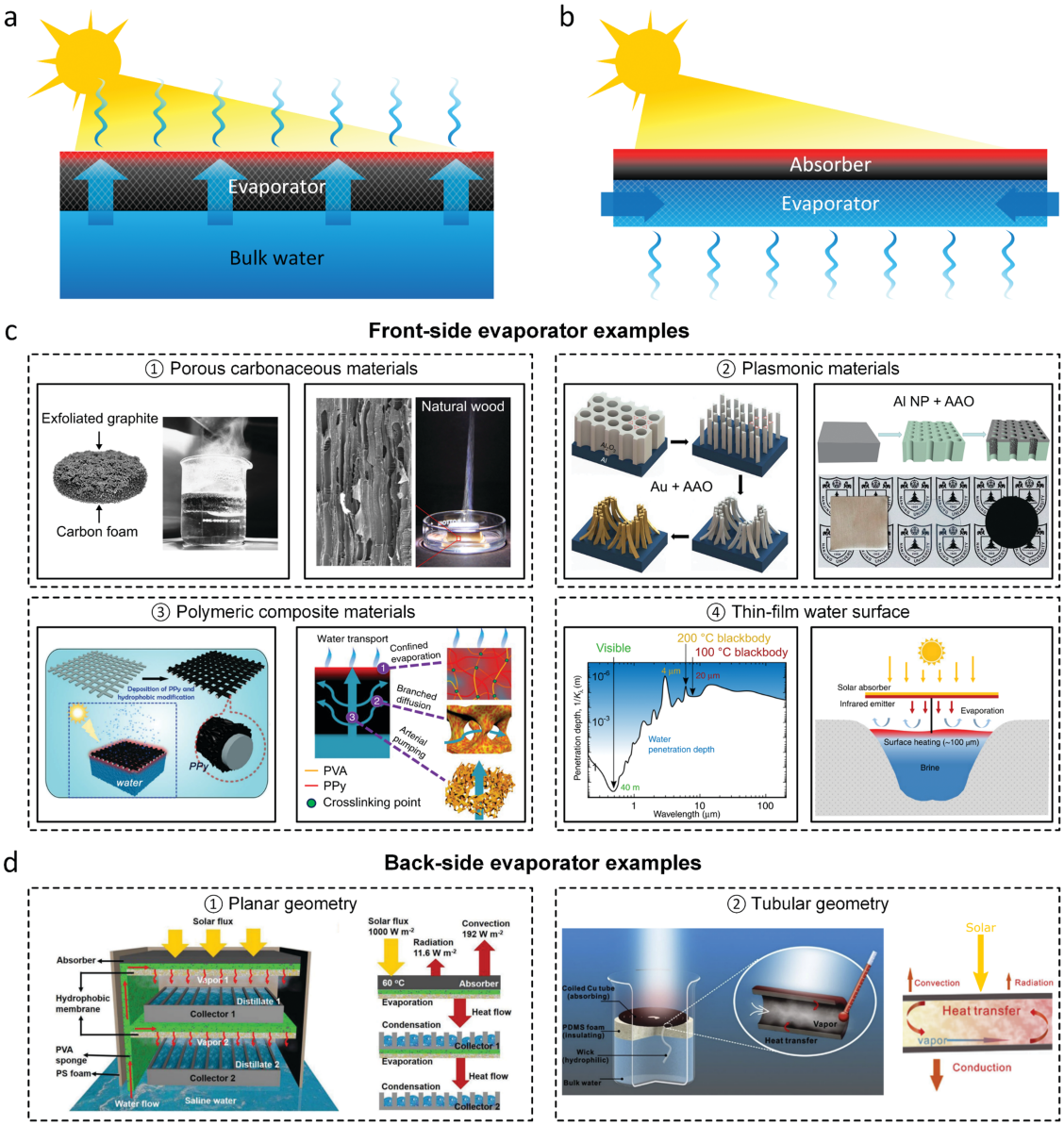

Fig. 2 Evaporator configurations utilizing thermal localization. (a) Schematic representing the front-side configuration where evaporation and solar absorption occur on the same side. (b) Schematic representing the back-side configuration where evaporation and solar absorption occur on opposite sides. (c) Representative front-side evaporators based on different materials. State-of-the-art front-side evaporators commonly employ porous carbonaceous (①),[26,49] plasmonic (②),[29,30] or polymeric (③) materials.[31,58] Reproduced with permissions from Springer Nature,[26,29–31] Elsevier,[49] and John Wiley and Sons.[58] Contactless solar vapor generation (④) uses the water surface, with its small penetration depth (~10 μm) in the infrared, as a thin-film absorber.[63,64] Reproduced with permissions from Springer Nature.[63,64] (d) Representative back-side evaporator designs based on planar (①)[65] and tubular geometries (②).[66] Reproduced with permissions from John Wiley and Sons[65] and Elsevier.[66]

since water vapor escapes from the front surface and can interfere with the solar absorption process – discussed in Section 3.1. Lastly, it is difficult to suppress heat loss from the absorber surface, *e.g.*, by applying thermal insulation such as a convection cover, without affecting vapor transport since solar absorption and evaporation occur on the same side.

The alternative back-side configuration, where the front surface is only used for solar absorption, decouples the competing demands of multiple functionalities in the front-side configuration and therefore allows a greater choice of absorber and evaporator materials, and geometries (Fig. 2d).[15,34,35,65–68] For instance, the absorber could simply comprise commercially available spectrally selective surfaces,[15,28,34] low-cost black paints,[69] and even photovoltaic (PV) cells.[35] Meanwhile, the evaporators could utilize conventional low-cost wicking materials without specific optical properties such as fabric[70] and paper.[34,69,71] In addition to the material choice flexibility, the back-side configuration offers two additional benefits for desalination applications – (1) it is easier to integrate with a vapor condenser or collector on the evaporator side since it does not interfere with solar absorption, and (2) it allows better heat loss suppression since it is easier to apply a convection cover or an optically selective shield to reduce the

convective and radiative heat loss from the absorber surface without affecting the evaporation process. We discuss the application of back-side evaporator in high-performance desalination devices in Sections 3.2 and 3.3.

2.2. Factors limiting evaporator performance

The design of high-efficiency evaporators warrants a clear understanding of the solar-vapor conversion process and identification of factors limiting its performance. In this section, we analyze the three key aspects of evaporator operation – heat loss, coupling of heat and mass transport, and water transport – which leads to the discussion of evaporator design bottlenecks and corresponding optimization strategies in Section 2.3.

In addition to the conventional definition given by eqn (1), the solar-vapor conversion efficiency can also be defined based on the total heat loss q''_{loss} using an energy balance,

$$\eta = 1 - \frac{q''_{loss}}{q''_{sun}} = 1 - \frac{h_{loss}\Delta T}{q''_{sun}} \quad (2)$$

where h_{loss} is the total heat loss coefficient which accounts for losses due to conduction, convection and radiation. $\Delta T = T_s - T_\infty$ is the superheat between the evaporator temperature T_s and the far-field ambient temperature T_∞. The effect of sensible heating is neglected in eqn (2). Fig. 3a shows the solar-vapor conversion efficiency as a function of the total heat loss coefficient and evaporator superheat temperature according to eqn (2). As h_{loss} or ΔT increases, η decreases due to higher heat loss. The red-dashed box marks the typical operating regime for devices reported in the literature with solar-vapor conversion efficiency ranging from $\approx$ 30% to $\approx$ 90%. Realizing solar-vapor conversion efficiency $>$ 90% requires not only an ultralow h_{loss} (*e.g.*, $\approx$ 5–10 W m^{-2} K^{-1}) but also a relatively low ΔT (*e.g.*, $\approx$ 5–15 °C) which is challenging, especially considering the fact that convective heat loss coefficient h_{conv} is already 5–15 W m^{-2} K^{-1} in a quiescent ambient air.[72–74] The most effective path to optimize evaporator performance should be along the trajectory A–B in Fig. 3a where h_{loss} and ΔT are reduced simultaneously. However, conventional approaches that rely on improving thermal insulation can only decrease h_{loss} and inevitably increase ΔT, following an optimization path along C–D (Fig. 3a) which leads to relatively limited enhancement in η. To realize low-superheat-temperature operation of a well-insulated evaporator, it is important to consider the vapor transport characteristics which determine both ΔT and h_{loss}.

Another key factor limiting the vapor generation performance is the coupling of heat and mass transport. Similar to most studies on evaporator design, we consider an evaporator as an open system, *i.e.*, vapor transport is from the evaporator to the far-field air ambient.[72–76] According to the energy balance, the total input solar energy Q_{sun} (units: W) is converted into thermal energy driving evaporation Q_{evap} and heat loss Q_{loss},

$$Q_{sun} = Q_{evap} + Q_{loss} = S_{evap}D_a h_{fg}(c_{sat}(T_s) - \phi_\infty c_{sat}(T_\infty)) + Ah_{loss}\Delta T \quad (3)$$

where S_{evap}, D_a, and A are the evaporative shape factor, vapor mass diffusivity in air, area of the evaporator, respectively. $c_{sat}(T_s)$ and $c_{sat}(T_\infty)$ are vapor saturation concentrations at T_s and T_∞, respectively. ϕ_∞ is the far-field relative humidity. In the diffusion limit, heat flow due to evaporation Q_{evap} is determined by the evaporative shape factor S_{evap} and vapor concentration gradient between the evaporator and far-field air ambient $\Delta c = c_{sat}(T_s) - \phi_\infty c_{sat}(T_\infty)$ according to Fick's law.[72,73,75] S_{evap} is only a function of the evaporator geometry and is related to the effective boundary layer thickness for vapor transport through $\delta = A/S_{evap}$. Smaller δ indicates better vapor transport and therefore leads to lower ΔT under steady-state

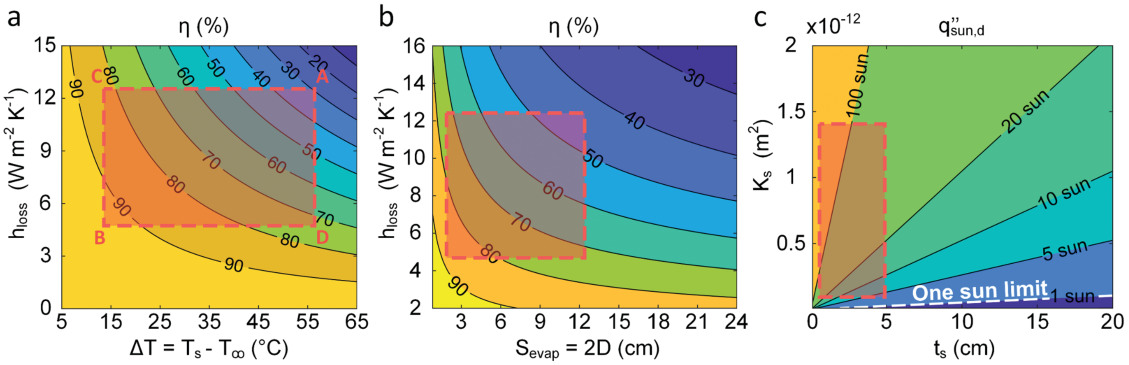

Fig. 3 Factors limiting evaporator performance – heat loss, coupled heat and mass transfer, and water transport. (a) Solar-vapor conversion efficiency η as a function of heat loss coefficient h_{loss} and evaporator superheat temperature ΔT. Higher η can be achieved by reducing h_{loss} and ΔT. The red-dashed box indicates the operation regime for typical evaporators. The ideal optimization path should follow the trajectory A–B, whereas improving the thermal insulation alone shifts the device operation along the trajectory C–D which improves the evaporator performance marginally. (b) Solar-vapor conversion efficiency η of a circular-disk evaporator (diameter D) as a function of heat loss coefficient h_{loss} and evaporative shape factor S_{evap} when T_∞ is 20 °C. S_{evap} is only a function of the evaporator geometry; $S_{evap} = 2D$ for a circular-disk evaporator. A smaller evaporator leads to better solar-vapor conversion efficiency due to smaller vapor transport resistance. The red-dashed box indicates the operation regime for typical evaporators. (c) Critical solar flux for evaporator dryout $q''_{sun,d}$ as a function of effective permeability K_s and capillary wick thickness t_s when the receding contact angle $\theta_{rec} = 15°$ and pore radius $r_{wick} = 100$ μm. The red-dashed box indicates the operation regime for typical evaporators, and the white-dashed line shows the one-sun limit. The water transport capability is typically not a bottleneck for the evaporator design due to the dilute nature of solar flux.

operation. Eqn (3) indicates that material design does not influence vapor transport because it only depends on evaporator geometry and thermal properties of vapor and air – also discussed by Patel *et al.*[12] To illustrate this point, we consider a circular disk evaporator with a diameter D and, therefore, a shape factor $S_{evap} = 2D$.[72,73] Fig. 3b shows the solar-vapor conversion efficiency η, calculated using Eqn (3), as a function of total heat loss coefficient and evaporation shape factor when T_∞ is 20 °C. η increases as S_{evap} decreases due to improved vapor transport and resulting reduction in ΔT. For a circular disk evaporator, since $\delta \sim D$, better vapor generation performance can be achieved using a smaller evaporator (Fig. 3b). The red-dashed box in Fig. 3b indicates an operation regime representative of recent literature. Due to the coupling of heat and mass transport, achieving solar-vapor conversion efficiency above 90% is challenging – consistent with our heat loss analysis shown in Fig. 3a. Additionally, this analysis raises a critical concern about the scalability of evaporator as it transitions from the laboratory small-scale ($D \sim 1$ cm) to the practical scale ($D \sim 1$ m), at least under the diffusion limit, which should be carefully investigated in future studies. On the other hand, the above analysis also demonstrates that there is a significant opportunity space to further improve the solar-vapor conversion efficiency by engineering the evaporator geometry or external air flow to reduce the effective boundary layer thickness for vapor transport.

The ability of the evaporator to transport water is another factor limiting evaporator performance, particularly because capillary driven flow enables passive solar thermal desalination. When the maximum liquid water supply rate of the capillary wick is less than the required evaporation rate, dryout occurs and the evaporator cannot generate more vapor. Liquid transport in the capillary wick can be described by Darcy's law and capillary pressure can be evaluated using the Young–Laplace equation.[73] Substituting the Young–Laplace equation into Darcy's law and considering one-dimensional (1D) liquid transport in the front-side configuration, the critical solar flux $q''_{sun,d}$ inducing evaporator dryout can be estimated as,

$$q''_{sun,d} = \frac{2h_{fg}\rho_l K_s}{\mu_l}\frac{\gamma\cos\theta_{rec}}{t_s r_{wick}} \quad (4)$$

where ρ_l, K_s, μ_l, γ, θ_{rec}, t_s, and r_{wick} are the density of the liquid, effective permeability of the wick, dynamic viscosity of the liquid, liquid–vapor surface tension, receding contact angle, thickness of the capillary wick and pore radius of the wick, respectively. Fig. 3c shows the critical solar flux as a function of effective permeability and capillary wick thickness when the receding contact angle is 15° and pore radius is 100 μm. The red-dashed box in Fig. 3c shows the operation regime for typical capillary wicks used in solar-vapor generation, which is above the one sun limit (*i.e.*, 1000 W m^{-2}, white-dashed line in Fig. 3a). Therefore, the water transport capability is usually not a bottleneck. However, when concentrated sunlight (*e.g.*, larger than 10 suns) is used for vapor generation, water transport could become a limiting factor and material-level innovations could help avoid evaporator dryout. Note that the critical solar flux estimated by eqn (4) is valid for front-side evaporators. For the back-side configuration, where the water is mainly supplied from the side of the evaporator, the corresponding critical solar flux can be lower than the value predicted by eqn (4), and materials engineering to improve water transport could be important. However, for back-side evaporators operated under dilute solar flux (*e.g.*, one sun illumination), recent experimental studies show that water transport capability is still not a primary limiting factor.[28,34,67,70]

2.3. Thermal management strategies for optimizing evaporator performance

Since heat loss and vapor transport are two dominant factors affecting solar-vapor conversion efficiency, here we discuss specific thermal management strategies used to optimize coupled heat and mass transport. Fig. 4a shows a schematic of the heat and mass transport for a front-side evaporator. The total heat loss is mainly attributed to thermal radiation (Q_{rad}), convection (Q_{conv}) from the top of the evaporator and heat conduction (Q_{cond}) to the bulk water. Accordingly, there are three thermal management strategies applied to reduce heat loss in practice. Spectrally selective solar absorbers, which have high absorptance in the solar spectrum (wavelength $\approx$ 0.3–3 μm) but low emissivity in the infrared (wavelength $>$ 3 μm), are used in high-performance evaporators to reduce radiative losses. Fig. 4b shows a representative spectrum for a selective absorber which significantly reduces thermal radiation losses in the infrared (the shaded dark-red area) compared with a blackbody absorber at 50 °C (the shaded grey area) due to its low emissivity (= 0.05).[28] Fig. 4c and d show examples of front-side and back-side evaporators that used commercially available spectrally selective absorbers to minimize radiative losses.[28,34] Convective heat losses from the absorber surface are typically suppressed using a convection cover, which is a highly solar-transparent material with low thermal conductivity, such as glass, air gap, bubble wrap, and silica aerogel.[15,28,34,77–79] The high-performance convection cover can also be opaque to infrared radiation (*e.g.*, silica aerogel), which further reduces the radiative loss from the absorber.[78] In the examples shown in Fig. 4c and d, low-cost bubble wrap and silica aerogel constituted the convection covers.[28,34] Note that for solar absorbers operating at high temperatures ($\approx$ 100 °C or even higher) under solar concentration,[29,30,80,81] thermal concentration,[28,82] or contactless heating,[63,64] it is particularly important to use spectrally selective solar absorbers and convection covers to maximize the solar-vapor conversion efficiency.[78] To minimize heat loss from the evaporator to bulk water, it is also necessary to reduce conduction heat transfer. For the front-side configuration, the conduction barrier is typically a low-thermal conductivity wick or foam (Fig. 4c).[26,28,70] Whereas for the back-side configuration, the conduction barrier is realized by reducing the contact area between the evaporator and bulk water, *e.g.*, by converting surface contact (Fig. 4c) to a line contact (Fig. 4d).[15,34,35,67,68,83]

To quantitatively compare the impact of each thermal management strategy on solar-vapor conversion efficiency, we refined the heat and mass transport analysis in eqn (3) by including the radiative, convective, and conductive heat loss

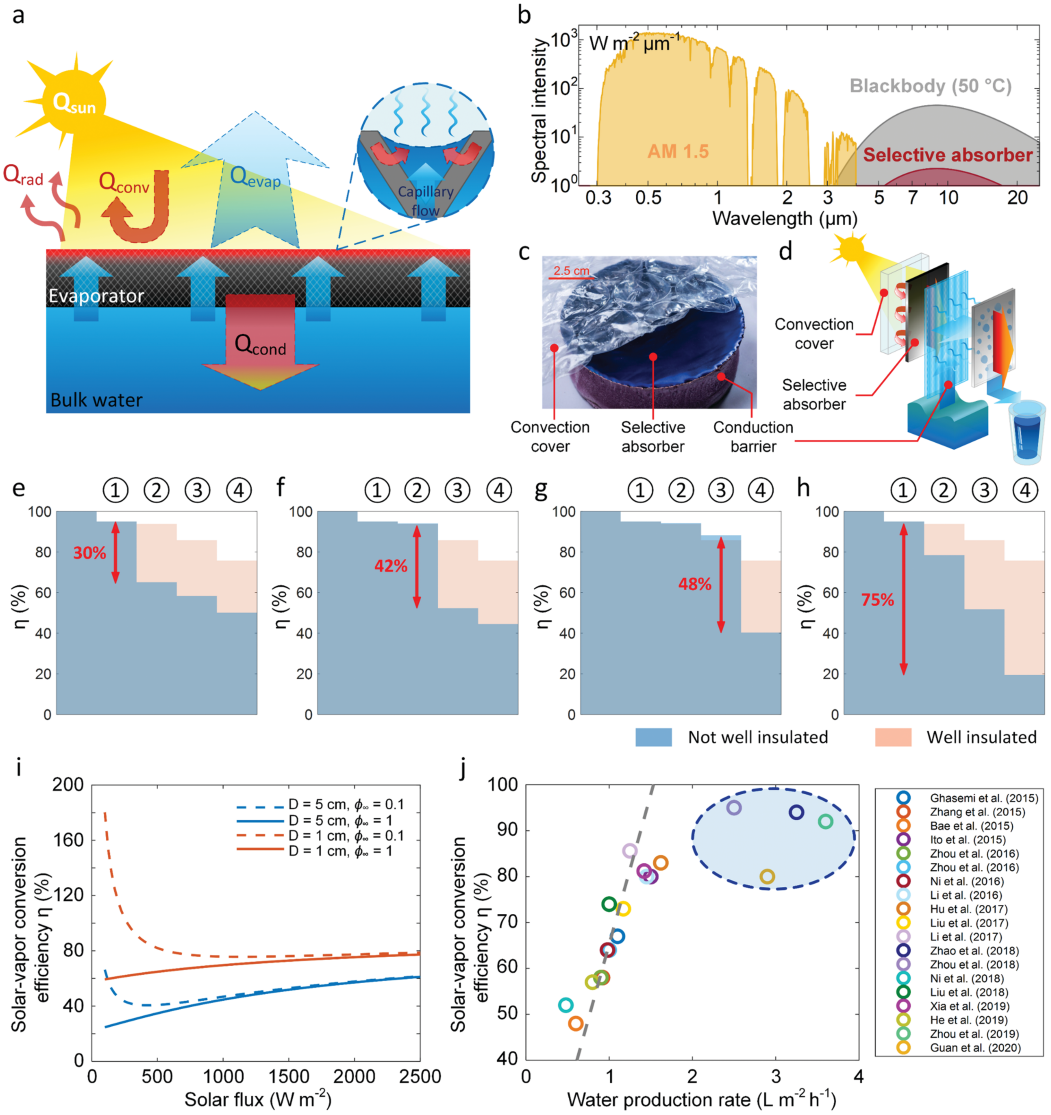

Fig. 4 Thermal management strategies for optimizing the evaporator performance. (a) Schematic showing heat and mass transport contributions for a front-side evaporator. The input solar energy Q_{sun} is converted into evaporative heat flow Q_{evap}, radiative heat loss Q_{rad}, convective heat loss Q_{conv}, and conductive heat loss Q_{cond}. Inset: Passive liquid transport driven by capillary pressure of the liquid–vapor interface in the porous structure of the evaporator. Solar energy is absorbed and converted into heat by the solid part of the wick. Heat is transferred from the solid structure to the liquid inside the pore through the solid–liquid interface to drive evaporation. (b) AM 1.5 standard solar spectrum and blackbody spectrum at 50 °C. The dark-red area represents the thermal radiation spectrum of a modeled spectrally selective absorber with infrared emissivity of 0.05 at 50 °C. (c) and (d) Representative thermally-localized (c) front-side and (d) back-side evaporators using spectrally selective absorber, convection cover and conduction barrier as thermal insulation.[28,34] Reproduced with permissions from Springer Nature (c)[28] and Royal Society of Chemistry (d).[34] In the design shown in (c), a bubble wrap and a low thermal conductivity foam are used as the convection cover and conduction barrier, respectively. In the design shown in (d), a transparent silica aerogel is used as the convection cover and reduced contact between the bulk water and the evaporator minimizes conduction. (e)–(h) Reduction of solar-vapor conversion efficiency η due to ① imperfect absorption, ② radiative heat loss, ③ convective heat loss, and ④ conductive heat loss. Comparison between a well-insulated evaporator (pink background in (e)–(h)) and a not well-insulated evaporator (blue area in (e)–(h)) by removing (e) spectrally selectivity of the absorber, (f) convection cover, (g) conduction barrier and (h) all thermal insulation. Significant loss in solar-vapor efficiency is observed when thermal insulation is removed. The evaporator is modeled as a circular disk with diameter D = 5 cm, thickness t_s = 3 cm and solar absorptance α = 0.95. The ambient temperature T_∞ = 20 °C. For the well-insulated case, the infrared emissivity of solar absorber, total convective loss coefficient, and effective thermal conductivity of the capillary wick are ε = 0.03, h_{conv} = 1.5 W m^{-2} K^{-1}, and k_{wick} = 0.06 W m^{-1} K^{-1}, respectively. ε = 0.95, h_{conv} = 10 W m^{-2} K^{-1}, and k_{wick} = 0.6 W m^{-1} K^{-1} are used to represent the conditions without a spectrally selective absorber, convection cover, and conduction barrier, respectively. (i) Effect of mass transport on the solar-vapor conversion efficiency η as a function of solar flux, modeled using representative circular disk evaporators with diameters D = 1 cm and D = 5 cm under low relative humidity ϕ = 0.1 and saturated conditions ϕ = 1. The convective loss coefficient is h_{conv} = 10 W m^{-2} K^{-1}. Smaller size evaporator has better performance due to the reduced vapor transport resistance. The dashed and solid lines show the solar-vapor conversion efficiency with/without the contribution of dark evaporation. Dark evaporation contributes significantly to the total vapor generation at the low solar flux regime ($<$ 200 W m^{-2}) whereas it becomes negligible when the solar flux is larger than 1500 W m^{-2}. (j) A compilation of solar-vapor conversion efficiencies η and corresponding water production rates reported by recent studies using the thermal localization approach.[26,28–32,46,48,51,53,55,58,59,70,80,84–87] Solar-vapor conversion efficiency is usually proportional to water production rate as indicated by the grey-dashed line, since latent heat of water is nearly constant. The results highlighted in the blue-dashed area represent recent studies using hydrogel[31,32,59] and bacterial cellulose nanocomposites[87] which report higher water production rates due to a reduction in latent heat of water.

contributions for a front-side evaporator configuration,

$$A\alpha q''_{\text{solar}} = S_{\text{evap}} D_a h_{fg} \Delta c + A\varepsilon\sigma\left(T_s^4 - T_\infty^4\right) + Ah_{\text{conv}}\Delta T + \frac{\Delta T}{\frac{1}{S_{\text{cond}}k_l} + \frac{t_s}{Ak_{\text{wick}}}} \quad (5)$$

where α, ε, σ, h_{conv}, k_l, and k_{wick} are the evaporator solar absorptance, evaporator infrared emissivity, Stefan–Boltzmann constant, convective heat loss coefficient, water thermal conductivity, and effective thermal conductivity of the capillary wick, respectively. $S_{\text{cond}} = 2D$ is the conductive shape factor for a circular-disk evaporator.[72,73] $h_{\text{conv}} = 1/(1/h_a + 1/h_c)$ includes the contributions of both the heat transfer coefficient of air ambient (h_a) and convection cover (h_c). For simplification, the solar and infrared transmittance of the convection cover are not included in the analysis. Note that eqn (5) provides a general modeling framework to guide the quantitative design of solar-vapor generation under the diffusion limit, where the impact of different thermal management strategies can be understood by solving eqn (5). A more in-depth discussion about modeling of evaporation can be seen in our recent perspective paper.[73] The key difference between eqn (5) and other energy balance analysis is that the evaporative transport coefficient, which was an empirical value in previous analysis, can be analytically determined through the evaporative shape factor, therefore leading to a rigorous coupling of heat and mass transport and quantitative prediction for the effect of different thermal management strategies. Eqn (5) should provide reasonable predictions for small scale devices ($\sim$ cm) operated at a relative low temperature ($<$ 100 °C) in a quiescent air ambient where the diffusion limit condition is held. Note that when the external flow field (due to natural convection or natural wind) becomes significant, the diffusion limit assumption is invalid. Therefore, additional theoretical efforts are required to understand the resulting coupling between mass transport and fluid flow.

We use the heat and mass transfer framework given by eqn (5) to analyze the relationship between different loss mechanisms and resulting solar-vapor conversion efficiency. In the results presented in Fig. 4e–h, four loss mechanisms are considered for an evaporator with D = 5 cm and t_s = 3 cm under one sun illumination with imperfect solar absorption (α = 0.95, ① in Fig. 4e–h), radiative loss (② in Fig. 4e–h), convective loss (③ in Fig. 4e–h), and conductive loss (④ in Fig. 4e–h). Fig. 4e–h show how the solar-vapor conversion efficiency decreases due to each loss mechanism. The pink background indicates a reference condition with relatively good thermal insulation (ε = 0.03, h_{conv} = 1.5 W m^{-2} K^{-1}, and k_{wick} = 0.06 W m^{-1} K^{-1}) while the blue regions represent cases without spectrally selectivity ($\varepsilon = \alpha$ = 0.95, Fig. 4e), without convection cover ($h_{\text{conv}} = h_a$ = 10 W m^{-2} K^{-1}, Fig. 4f), without conduction barrier ($k_{\text{wick}} = k_l$ = 0.6 W m^{-1} K^{-1}, Fig. 4g), and without any thermal insulation (ε = 0.95, h_{conv} = 10 W m^{-2} K^{-1}, and k_{wick} = 0.6 W m^{-1} K^{-1}, Fig. 4h). Imperfect solar absorption (α = 0.95) leads to a 5% reduction in solar-vapor conversion efficiency (① in Fig. 4e–h). The results of this analysis show that spectrally selective absorber, convection cover and conduction barrier are all essential to achieve a high efficiency. Specifically, in comparison with the well-insulated case, the absence of absorber spectral selectivity reduces η by 30% (② in Fig. 4e). Directly exposing the evaporator to the air ambient without a convection cover could reduce η by more than 40% due to convection (③ in Fig. 4f). Suppressing conductive loss through bulk water is comparatively more important and could cause η to reduce by 50% if the conduction barrier is removed (④ in Fig. 4g). If no thermal insulation is applied, more than 75% of the incident solar energy would be lost to the environment which leads to η less than 20% (Fig. 4h). This analysis highlights the significance of optimizing thermal transport to reduce h_{loss} and increase η.

In addition to thermal transport, mass transport can also have a significant impact on solar-vapor conversion efficiency. For evaporation to the far-field air ambient under the diffusion limit, vapor transport is governed by two parameters according to eqn (3) and (5) – the evaporator geometry (diameter D) and the far-field condition (relative humidity ϕ_∞). A smaller evaporator results in a smaller effective boundary layer thickness δ, leading to a smaller vapor transport resistance. When the vapor in the far-field is not saturated (*i.e.*, $\phi_\infty < 1$), evaporation can still occur even in the absence of a temperature difference between the evaporator and air ambient (*i.e.*, $\Delta T = T_s - T_\infty$ = 0 °C) because the concentration gradient $\Delta c = c_{\text{sat}}(T_s) - \phi_\infty c_{\text{sat}}(T_\infty) = (1 - \phi_\infty)c_{\text{sat}}(T_\infty)$ is greater than zero. This evaporation phenomenon without any input solar flux is known as dark evaporation[11,73] or evaporation harnessing environmental energy.[61] Dark evaporation increases the total vapor production but is typically removed from calculations of solar-vapor conversion efficiency by careful experimental calibration, since it is not a solar-induced process and is highly dependent on far-field weather conditions.[73] The total measured vapor generation rate under a non-saturated far-field condition is the sum of the evaporation rate under a saturated condition and the dark evaporation rate, because $Q_{\text{evap}} \sim c_{\text{sat}}(T_s) - \phi_\infty c_{\text{sat}}(T_\infty) = [c_{\text{sat}}(T_s) - c_{\text{sat}}(T_\infty)] + [(1 - \phi_\infty)c_{\text{sat}}(T_\infty)]$. Fig. 4i shows the solar-vapor conversion efficiency as a function of solar flux for different evaporator diameters and far-field conditions. As expected, a smaller evaporator performs better due to smaller vapor transport resistance. The solid line in Fig. 4i is the solar-vapor conversion efficiency without dark evaporation. If we include the dark evaporation contribution (the dashed lines in Fig. 4i), it significantly increases the solar-vapor conversion efficiency at a low solar flux ($<$ 200 W m^{-2}) but has a negligible effect when the solar flux is greater than 1500 W m^{-2}. Since typical solar evaporators are operated under a low solar flux condition ($<$ 1000 W m^{-2}), the contribution of dark evaporation should be carefully calibrated and can be used to increase the overall evaporation rate. As shown in Fig. 4i, careless calibration could lead to a solar-vapor conversion efficiency greater than 100% since dark evaporation is not driven by solar energy. To accurately calibrate dark evaporation, the evaporator shape factor (including the configuration of the evaporator relative to the water surface and reservoir) and the

far-field conditions (including the far-field temperature and relative humidity) should be the same for both experiments – with and without solar illumination. Note that although evaporation to air ambient can take advantage of dark evaporation to drive more vapor generation, it has no effect on evaporation in a closed system which is commonly used for desalination devices – discussed further in Section 3.

Advances in thermal management approaches have led to improvements in solar-vapor conversion efficiency and water production rates reported by recent studies (Fig. 4j).[26,28–32,46,48,51,53,55,58,59,70,80,84–87] The reported studies used thermal localization to achieve solar-vapor conversion efficiencies greater than 50%. By incorporating thermal management strategies discussed above, the demonstrated η can be as high as 90% with more than 1.5 L m^{-2} h^{-1} water production rate under the one sun illumination. The solar-vapor conversion efficiency is typically linearly related to the water production rate (the dashed-grey line in Fig. 4j) since the latent heat of water is almost a constant ($\approx$ 2400 kJ kg^{-1}). However, several recent studies show that it is possible to produce more than 2.5 L m^{-2} h^{-1} of water using hydrogel[31,32,59] and bacterial cellulose nanocomposites,[87] which indicates a reduction of water latent heat during evaporation (the blue-dashed circle in Fig. 4j). These novel materials offer a new pathway for efficient vapor and water generation; more theoretical and experimental evidence is, however, required to explain the underlying mechanism for the reduction of latent heat. In particular, according to eqn (5), the high evaporation rate with reduced latent heat also indicates an increased vapor pressure or a reduced mass transport resistance. Therefore, it is of great interest to understand the underlying physics of the hydrogel evaporator from the perspective of mass transport in future works.

Using our analysis in this section, we show that optimizing heat and mass transport at the device level is crucial for high-performance evaporator design. On the other hand, further research on advanced materials has relatively limited impact on enhancing the energy efficiency unless those materials fundamentally change the thermodynamic properties (such as latent heat) of water.[7,12,13] Diverse thermal management strategies such as spectrally selective absorber, convection cover and conduction barrier have already led to significant reductions in heat loss. Future advances could be enabled by optimizing vapor transport by engineering the geometry of the evaporator or the external flow field. In addition, modeling tools that account for the complex coupling of heat and mass transport with fluid flow could facilitate optimization and quantify the performance of laboratory scale prototypes as well as large-scale industrial setups.

3. Design of high-performance solar desalination devices using thermal localization

A passive solar desalination device can be constructed by integrating an evaporator with a condenser in a closed system. In this section, we highlight the recent progress in solar desalination device designs based on thermally-localized evaporators. We analyze different configurations and underlying heat and mass transport characteristics, which have led to significant improvements in the performance of solar desalination devices. In particular, we show that the efficiency of a desalination device is not strongly correlated with the performance of the evaporator in an open system due to the significantly different heat and mass transport mechanisms. Furthermore, we discuss the extension of desalination device designs from single-stage to multistage devices, which have shown multifold enhancement in water production rates through latent heat recycling during vapor condensation.

3.1. Single-stage solar desalination device configurations

Single-stage desalination devices can be characterized based on the configuration of their evaporators – front-side or back-side. Fig. 5a shows the schematic of a desalination device with a front-side evaporator, where the condenser is placed between the evaporator and incident sunlight due to the vapor flow direction. The condenser should be solar transparent to ensure the sunlight reaches the absorber. Alternatively, the desalination device can be also constructed using a back-side evaporator, where the condenser is placed on the opposite side of incident sunlight, behind the evaporator (Fig. 5b). Fig. 5c–f show a few examples of single-stage desalination devices from literature.[31,69,70] These demonstrations primarily used front-side evaporators where a transparent cover (acrylic – Fig. 5c or polyester film – Fig. 5e) serves as the condenser and the condensed droplets are removed by gravity. In addition to the advantages discussed in Section 2.1, desalination devices using back-side evaporators offer three additional benefits. First, in comparison with front-side devices which severely restrict the choice of condenser materials due to the requirements of solar transparency and relatively high thermal conductivity, back-side devices allow the use of a wide range of materials for condensation including common low-cost metals such as copper and aluminum.[34,77] Moreover, additional cooling, *e.g.*, through direct contact of the condenser back-side with water, can be easily implemented to further enhance vapor condensation.[15,34] Second, the back-side design eliminates the loss of input solar energy due to the condenser positioned in front of the evaporator in front-side devices (Fig. 5g), where the incident sunlight can be further reduced due to backscattering by the condensed droplets.[88] Third, the single-stage desalination device based on the back-side evaporator can be easily upgraded to a multi-stage device using a modular design (discussed in Section 3.3). On the other hand, as mentioned in Section 2.1, a potential drawback of the back-side design is the limited water transport capability due to the water supply from the side of the evaporator. Although it has been experimentally demonstrated that the water transport capability of the back-side desalination device is sufficient under dilute solar flux ($\approx$ 1000 W m^{-2}),[15,34,35,67,68] additional design constraints need to be considered for the back-side device operation under concentrated solar/thermal fluxes.

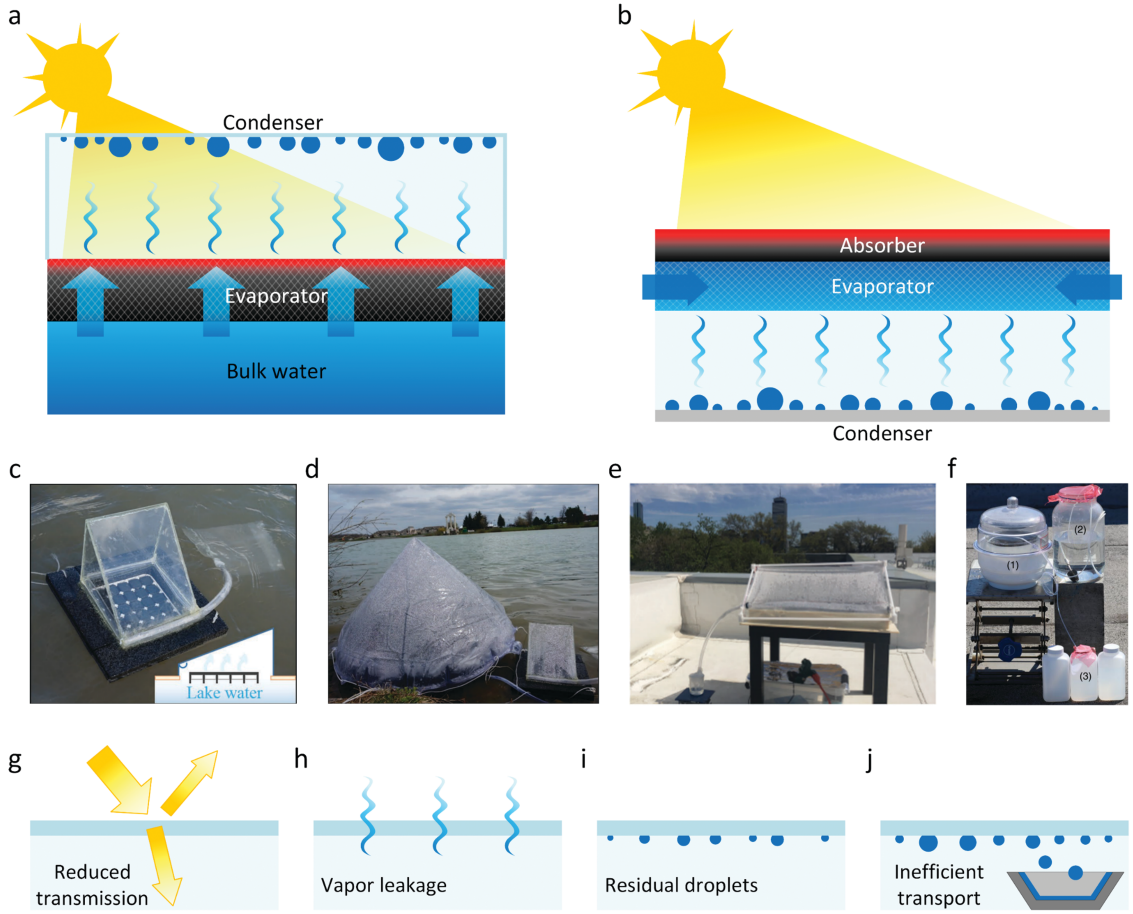

Fig. 5 Single-stage desalination device configurations based on thermally-localized evaporators. (a) and (b) Schematics of single-stage desalination device based on (a) front-side and (b) back-side evaporators. In the front-side device, a solar-transparent condenser is placed in front of the evaporator, allowing sunlight to reach the absorber. In the back-side device, the solar absorber directly faces the incident sunlight while the condenser is behind the evaporator. (c)–(f) Representative single-stage desalination devices using the front-side configuration shown in literature.[31,69,70] Reproduced with permissions from John Wiley and Sons (c and d),[69] Royal Society of Chemistry (e),[70] and Springer Nature (f).[31] (g)–(j) Additional loss mechanisms during water desalination due to (g) reduced transmission through the condenser, (h) vapor leaking from the device, (i) droplets pinning on the condenser, and (j) inefficient water transport and collection.

The vapor condensation and water collection processes in desalination devices introduce additional losses, when compared with evaporation only. In addition to the optical loss due to the condenser and droplets in the front-side device (Fig. 5g), vapor leakage (Fig. 5h), residual droplets (Fig. 5i), and inefficient water transport and collection (Fig. 5j) in both the front-side and back-side devices due to imperfect sealing, droplet pinning,[89–91] and liquid film wetting,[92,93] respectively, could reduce the amount of collected fresh water.[34] Therefore, an airtight system with high droplet mobility, *e.g.*, using hydrophobic coatings[94–97] and efficient water transport[98–102] are critical to achieving high water production rates.

Losses in water collection also require more thoughts and considerations during experimental characterization. In studies measuring evaporator performance in an open system, the production rate is usually measured from the mass loss rate of the bulk water in a reservoir. However, since there are additional losses associated with desalination devices, the production rate given by the mass loss rate of the reservoir is higher than the actual desalinated water collection rate. Therefore, a more accurate measure of the desalination device performance would involve characterization of both the mass loss rate of the reservoir and the collection rate of desalinated water. The mass loss rate is a more fundamental property that shows the effect of heat and mass transport on vapor generation, whereas the actual water collection is a more practical standard to quantify the ultimate performance with all losses. The ratio of the water collection and reservoir mass loss shows the relative significance of imperfect water transport and collection for the overall desalination device design.

3.2. Heat and mass transport in a single-stage solar desalination device

This section focuses on the heat and mass transport characteristics and the resulting optimization strategy for a single-stage desalination device. We consider the back-side device as an example. Fig. 6a shows the heat and mass transport processes where the incident solar energy (Q_{sun}) is balanced by radiative

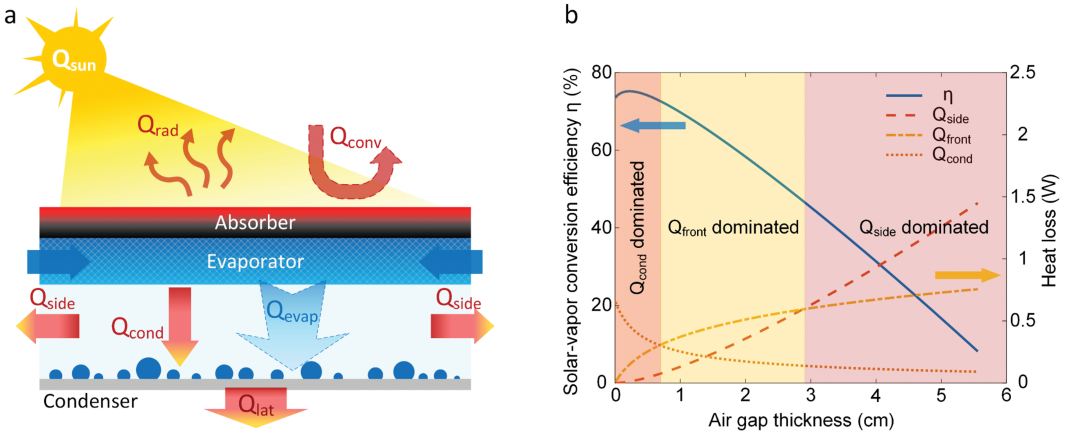

Fig. 6 Solar-vapor conversion in a single-state desalination device. (a) Schematic showing the heat and mass transport processes in a back-side single-stage desalination device. The air gap between the evaporator and condenser adds a tunable heat and mass transport resistance, which can significantly alter the evaporation and conduction processes compared to an evaporator in an open system. The vapor transport is not affected by the relative humidity of the ambient air because the vapor in contact with both the evaporator and condenser surfaces is in a saturated state. (b) Solar-vapor conversion efficiency η as a function of air gap thickness t_g for a modeled single-stage device. This desalination device is 5 cm × 5 cm in size and is operated at 20 °C ambient temperature. The simultaneous increase of vapor diffusion and heat conduction resistance with increasing air gap thickness leads to an optimal solar-vapor efficiency at about t_g = 0.3 cm. As t_g increases, the device spans three distinct regimes dominated by conductive, front-side, and side-wall heat losses. Note that this analysis considers an ideal process with no losses during water collection. Thus, the water production rate is equal to the vapor generation rate.

heat loss (Q_{rad}) and convective heat loss (Q_{conv}) from the absorber, and conductive heat loss (Q_{cond}) and evaporative heat flow (Q_{evap}) through the air gap between the evaporator and condenser. Heat loss from sidewalls (Q_{side}) due to convection can reduce the energy reaching the condenser. Vapor condenses on the condenser and releases latent heat (Q_{lat}), which is then lost to the environment. Although the vapor transport resistance can be reduced by creating a vacuum or pure vapor environment with pumping or evacuated tube, to ensure the passive operation and simple architecture, the vacuum or pure vapor environment is not commonly used in current small-scale solar desalination devices. Therefore, vapor transport within the air gap, driven by a concentration gradient between the hot evaporator and cold condenser, is described by the Fick's law. In a 1D condition, the evaporative heat flow rate is given by,[72,73]

$$Q_{evap} = AD_a h_{fg} \frac{(c_{sat}(T_s) - c_{sat}(T_c))}{t_g} \quad (6)$$

where T_c is the temperature of the condenser and t_g is the air gap thickness. Comparing eqn (6) with eqn (3), it can be seen that the mass transport in a desalination device is fundamentally different from that in an open system. The evaporative heat flux in a desalination device is determined by the saturated vapor concentration at T_s and T_c, and the relative humidity of the far-field ambient air has no impact on vapor transport. Therefore, vapor generation in desalination devices cannot benefit from the contribution of dark evaporation. In addition, the vapor transport resistance, which is a constant related to the evaporative shape factor for an open system, becomes broadly tunable through the air gap thickness. Specifically, the vapor transport resistance is infinitely large when t_g approaches infinity and is negligible when t_g is approximately zero. Similar to mass transport, conductive heat transfer from the evaporator to the condenser is also dominated by the air gap thickness. Due to this new design parameter (the air gap thickness), the performance of an evaporator in an open system is not a good indicator of its performance in a desalination device.

Fig. 6b shows the solar-vapor conversion efficiency as a function of air gap thickness for the modeled single-stage device. The modeled device area is 5 cm × 5 cm and ambient temperature is 20 °C. We assumed that the condenser is inserted in bulk liquid and therefore, the condenser temperature is maintained at T_c = 20 °C. The absorber temperature, and heat and mass flow rates are solved by substituting eqn (6) into the overall energy balance. Detailed modeling procedures and simulation parameters can be found in our recent work.[36] With increasing t_g, η first increases and then decreases, leading to an optimal gap thickness t_g = 0.3 cm (Fig. 6b). This optimal solar-vapor efficiency arises from the simultaneous increase of the vapor diffusion and heat conduction resistance with t_g. When the air gap is small (t_g < 0.7 cm), conduction through the air gap is the dominant heat loss. Therefore, even though reducing t_g below 0.3 cm decreases the vapor diffusion resistance, the resulting increase in conductive heat loss leads to a reduction in η for t_g < 0.3 cm. When 0.7 cm < t_g < 3 cm, the device transitions to a regime dominated by front-side heat loss Q_{front} ($Q_{front} = Q_{rad} + Q_{conv}$) due to the elevated temperature of the solar absorber. When t_g > 3 cm, heat loss from the sidewall becomes dominant mainly because of the large sidewall area. Significant increase in total heat loss leads to a rapid decay of η at large air gap thicknesses (t_g > 0.7 cm). The heat and mass transport for the front-side configuration follow principles similar to those described above, but require consideration of extra loss mechanisms discussed in Section 3.1.

3.3. Improving water production using latent heat recycling by a multistage design

Although heat and mass transport optimization and heat loss reduction during water collection significantly improve device performance, water production by a single-stage desalination device is inherently limited by the latent heat Q_{lat} lost to the ambient environment after vapor condensation (Fig. 6a). Therefore, the solar-vapor conversion efficiency of a single-stage device cannot exceed 100% (GOR = 1). Recently, multifold enhancement of solar-vapor conversion efficiency beyond 100% was demonstrated by recycling the latent heat using multistage device designs.[15,34,35,68,103,104] Fig. 7a shows a schematic of the multistage solar desalination device. This multistage design comprises a closely packed layered structure with several stages aligned with the incident sunlight (Fig. 7a). Liquid is supplied passively from the side of the device driven by capillary pressure. The evaporator in each stage is separated from the condenser by a hydrophobic membrane or an air gap.[15,34,35,68,103,104] During operation, the latent heat released from the previous stage is used to drive evaporation in the next stage, leading to more vapor and water production.

The concept of recycling latent heat is not new – it is a mature technology widely used in conventional large-scale and centralized thermal desalination systems such as multistage flash and multiple-effect distillation.[22,105–110] However, the successful implementation of latent heat recycling in small-scale passive desalination devices was only demonstrated recently.[15,34,35] Since the motivation and potential benefits of recycling latent heat have been carefully reviewed by Wang *et al.*,[7] we will focus on the design principle and opportunity space for high-performance multistage desalination devices. Fig. 7b shows the predicted solar-vapor conversion efficiency and water production rate as a function of the number of device stages N. The modeled multistage device with a 15 cm × 15 cm area and a 0.5 cm air gap thickness is operated at 20 °C ambient temperature and one sun illumination. The details of the modeling procedures can be seen in ref. 36. In this example, a greater than six-fold enhancement in solar-vapor conversion efficiency (*i.e.*, GOR > 6) over a single-stage device is predicted when $N > 20$ (Fig. 7b), which corresponds to a water production rate of about 10 L m^{-2} h^{-1}. Interestingly, η does not follow a linear trend (the grey-dashed line in Fig. 7b) with increasing N due to the accumulated sidewall heat loss from each stage. As a result, the benefit of adding one more stage keeps diminishing, leading to a plateauing of the achievable solar-vapor conversion efficiency (yellow regime in Fig. 7b). The yellow star at about N = 15 marks the approximate position where the plateauing occurs (less than 5% difference compared with the maximum solar-vapor conversion efficiency); the region before (green regime in Fig. 7b) represents the regime where increasing N is beneficial. Therefore, for a practical multistage design, the number of stages should be carefully chosen to balance the performance enhancement and material cost.

Fig. 7c–e show recent representative studies using the multi-stage approach to enhance solar desalination performance. Chiavazzo *et al.* developed a multistage device (Fig. 7c) with two hydrophilic layers separated by a hydrophobic microporous membrane as a single stage.[15] The two hydrophilic layers serve as the evaporator and condenser, respectively. The vapor-permeable hydrophobic layer separates the evaporator and the condenser and only allows vapor to transport through. They demonstrated a water production rate of 3 L m^{-2} h^{-1} using a ten-stage device.[15] Wang *et al.* designed and demonstrated a hybrid photovoltaic (PV) solar desalination device with multiple evaporation and condensation stages (Fig. 7d).[35] A commercial polycrystalline silicon solar cell is used as the solar absorber to convert short-wavelength photons to electricity and long-wavelength photons to heat. On the back of the solar cell, a three-stage evaporator–condenser unit is attached. The single-stage design is similar to Chiavazzo *et al.*'s work with a hydrophobic membrane separating two hydrophilic layers.[15,35] The hybrid device can generate electricity at 11% efficiency while producing portable water at 1.64 kg m^{-2} h^{-1} production rate.[35] Unlike previous works by Chiavazzo *et al.* and Wang *et al.*,[15,35] Xu *et al.* developed a simpler multistage device with higher water productivity (Fig. 7e).[34] In Xu *et al.*'s device, each single stage consists of a capillary wick (evaporator), an air gap, and a thin metal condenser. Instead of using a hydrophobic porous membrane, the air gap separates the evaporator and condenser while allowing water vapor to pass through. By optimizing the heat and mass transport processes, they demonstrated a record-high water production rate of 5.78 L m^{-2} h^{-1} with a ten-stage device.[34]

Similar to the single-stage device, heat and mass transport plays a critical role in the design of a multistage device. Our discussion in Section 3.2 is also valid for the multistage device, which should incorporate coupling between stages – outlined in the detailed modeling approach developed recently by Zhang *et al.*[36] Fig. 7f shows the effect of air gap thickness on the overall solar-vapor conversion efficiency of 15-stage and 30-stage modeled devices. Both devices have 15 cm × 15 cm area and are operated under one sun illumination. As the air gap thickness t_g increases, the solar-vapor conversion efficiency first increases and then decreases, passing through an optimal point at t_g = 0.3 cm. This optimal solar-vapor conversion efficiency is attributed to the transition from a heat transport (HT) limited regime (red region in Fig. 7f) to a mass transport (MT) limited regime (blue region in Fig. 7f). Specifically, when t_g is small (< 0.3 cm), heat conduction between the evaporator and condenser in each stage is significant, which leads to the heat transport limited regime. When t_g is large (> 0.3 cm), the mass transport resistance between the evaporator and condenser becomes the dominant resistance and the device transitions to the mass transport limited regime. The above analysis highlights the importance of in-depth modeling and quantitative optimization of the multistage device design.

We summarize the reported solar-vapor conversion efficiency of the state-of-the-art multistage designs in Fig. 7g.[15,34,35,65] Most designs with more than two stages can easily break the 100% efficiency limit of the single-stage design and therefore produce water at a rate over 2 L m^{-2} h^{-1}.[15,34,35] A comparison with the best performance predicted by modeling[36] indicates there exists

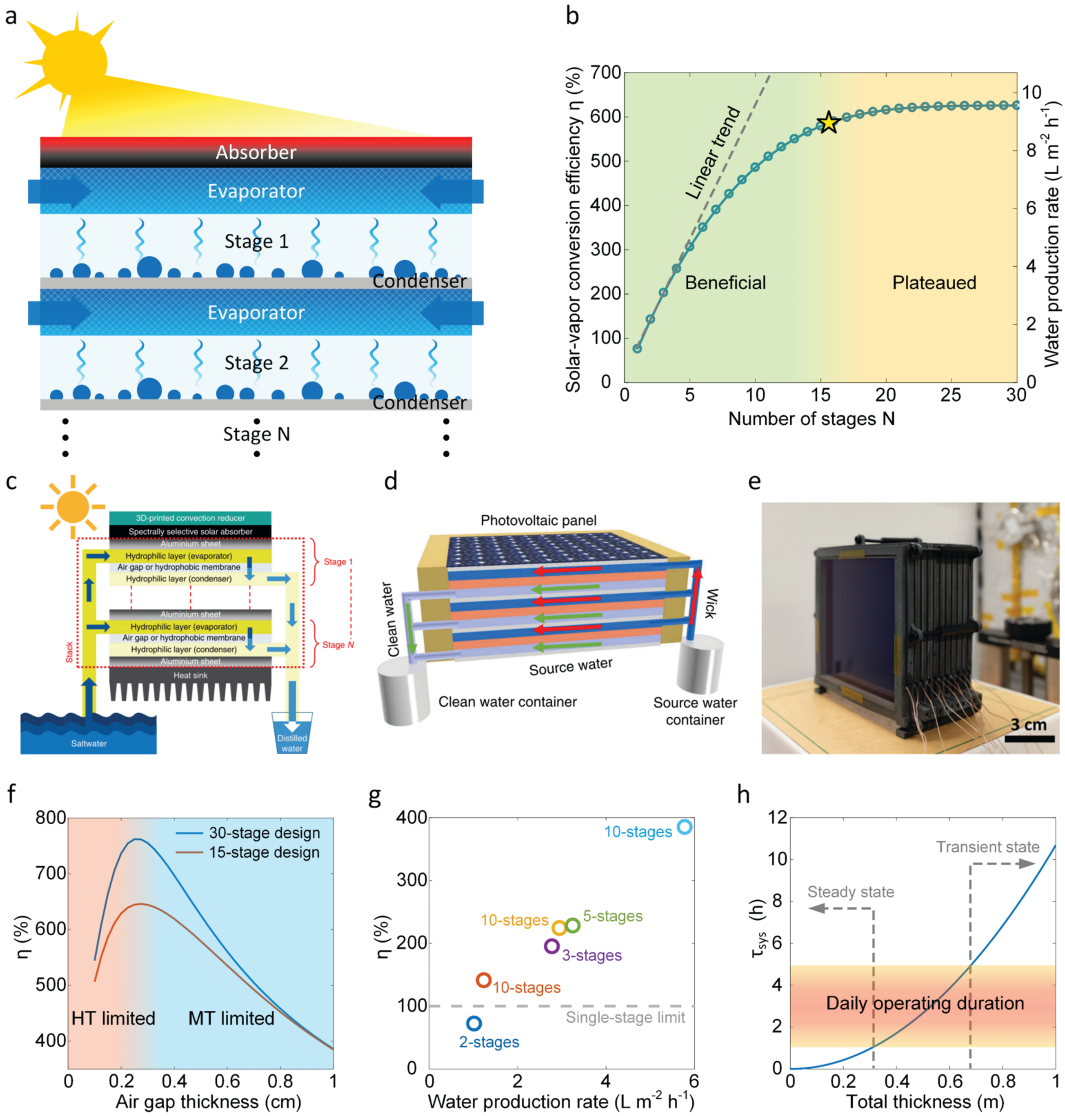

Fig. 7 Improving water production by recycling latent heat with a multistage design. (a) Schematic of a thermally-localized multistage solar desalination device showing the use of latent heat released in one stage to drive evaporation in the next stage. (b) Increase in solar-vapor conversion efficiency η and water production rate with the number of stages N. The water production rate and GOR in the modeled multistage device are predicted to increase by more than six times than that of a single-state device. The relative benefit of adding each additional stage diminishes with increasing N, leading to beneficial (green area in (b)) and plateaued (yellow area in (b)) regimes. The yellow star indicates the transition point beyond which the improvement of water production by increasing N becomes negligible. (c)–(e) Three representative demonstrations of the multistage design in recent studies.[15,34,35] Reproduced with permissions from Springer Nature (c and d)[15,35] and Royal Society of Chemistry (e).[34] Devices reported in (c) and (d) used hydrophilic membranes to evaporate water and hydrophobic membranes to transport vapor.[15,35] The device reported in (d) included a PV panel as the solar absorber and demonstrated simultaneous electricity and water production.[35] A record-high water production rate of 5.78 L m^{-2} h^{-1} was demonstrated in (e) by optimizing the heat and mass transport through the multistage structure.[34] (f) Solar-vapor conversion efficiency η as a function of single-stage air gap thickness for a 15-stage and a 30-stage device. As the air gap thickness increases, the device transitions from a heat transfer limited regime (red region in (f)) to a mass transport limited regime (blue region in (f)), leading to an optimal air gap thickness of about 0.3 cm. Note that this optimal air gap thickness is for the modeled device and conditions – 15 cm × 15 cm area device operated under one sun illumination and 20 °C ambient temperature. The general optimization procedures can be found in ref. 36. (g) Solar-vapor conversion efficiencies (η) and corresponding water production rates for various multistage devices reported by recent studies.[15,34,35,65] The grey-dashed line indicates the 100% efficiency limit for the single-stage device. (h) Thermal response time of the desalination device τ_{sys} as a function of the total thickness. τ_{sys} is estimated using t_{tot}^2/α_a, where t_{tot} is the combined thickness of all the layers and α_a is the thermal diffusivity of air.[72] The orange band ranging from 1 h to 5 h indicates the typical daily operation duration of the device based on the availability of solar radiation. When τ_{sys} is smaller than the lower bound of the daily operation duration, the device can reach steady state operation as indicated by the left-grey arrow. When τ_{sys} is larger than the upper bound of the daily operation duration, the device can never reach steady state as indicated by the right-grey arrow.

significant room for improving the multistage design, which requires optimization of the heat and mass transport. In terms of water production, pursuing the multistage design is a more rewarding direction compared with its single-stage

counterpart. However, the device cost per unit area of the multistage device could be much higher than that of the single-stage device due to the large number of stages, which might offset the performance benefits of the multistage design. Therefore, in addition to improving the water production, reducing the total cost with commercially available materials and simpler structures is of equal importance. We discuss the trade-off between the water production rate and device cost in Section 5.

Current theoretical and experimental investigations of multistage devices mainly focus on steady-state operation. However, the solar desalination device operation is inherently transient, because of the continuously changing solar flux from sunrise to sunset and the random fluctuations in solar flux and ambient temperature. When the response time of a desalination device is comparable to the characteristic time-scale of the above-mentioned transient factors, the dynamics of the device become important. Fig. 7h shows that the thermal response time τ_{sys} quadratically increases with the total thickness of a desalination device.[72] The daily operating duration of the device is typically one to five hours around the solar noon (the orange band in Fig. 7h). For a single-stage device which is thin (total thickness $\sim$ cm), τ_{sys} is much smaller than the daily operating duration and the device can rapidly reach steady state. However, for a full-scale multistage device, the total thickness could be large (*e.g.*, $\sim$ 10 cm to $\sim$ 1 m), which leads to a time constant comparable to the daily operating duration ($\sim$ h). Such a multistage device responds slowly and might never reach steady state during the period of operation. Since the slow thermal response will lead to both slow warm-up and cool-down processes of the desalination device, its impact on the overall water production compared to the steady state operation needs to be well-understood. In addition, large τ_{sys} also indicates a longer recovery time under the external perturbation of solar flux and ambient temperature due to the weather conditions. Therefore, an in-depth understanding of the transient behavior and dynamic response for the multistage device could be valuable for future high-performance solar desalination systems.

4. Designing anti-fouling, salt-rejecting and robust desalination devices

In addition to achieving a high production rate, a practical solar desalination device also needs to be reliable to ensure a long lifetime and reduce cost of maintenance. Fouling due to salt accumulation is one of the most common degradation mechanisms which blocks water transport and reduces the solar absorption area. In this section, we analyze salt transport during solar evaporation which helps identify the mechanisms causing salt accumulation and potential opportunities for effective salt removal. We also review state-of-the-art strategies for avoiding salt accumulation and accelerating salt rejection, which could enable desalination device designs with strong resistance to fouling.

4.1. Salt transport in thermally-localized solar desalination devices

Salt transport in the evaporator determines the salt accumulation and rejection rates. A clear understanding of salt migration dynamics during solar desalination is missing in the literature. In this section, we elucidate the physical mechanisms responsible for salt migration which show the complexity due to its transient, diffusive, and convective nature and its coupling with the temperature and flow field. Our analysis also illustrates why salt accumulation is a significant challenge for solar thermal desalination and highlights potential solutions to improve salt rejection by thermofluidic engineering.

The transport of salt ions is governed by the time-dependent convection–diffusion equation,[72,111]

$$\frac{\partial c}{\partial t} = D_{s,\mathrm{eff}}\nabla^2 c - \nabla\cdot(\boldsymbol{u}c) \tag{7}$$

where t, $D_{s,\mathrm{eff}}$, and $\boldsymbol{u}$ are the time, effective mass diffusivity of salt ions in the evaporator, and flow field, respectively. For a uniformly porous evaporator, salt diffusion can be reasonably estimated by $D_{s,\mathrm{eff}} = \varepsilon_p^{3/2} D_s$, where ε_p is the porosity of the evaporator and D_s is the intrinsic mass diffusivity of salt ions in water.[112–114] Fig. 8a shows the schematic of salt diffusion. At the liquid–air interface, water evaporates while dissolved ions remain in the liquid leading to a concentration gradient of dissolved ions along the capillary flow direction of the evaporator. Driven by this concentration gradient, ions diffuse from the interface to the low-concentration bulk water (Fig. 8a). However, due to the ultralow mass diffusivity of salt ions in water (*i.e.*, $D_s \sim 10^{-9}$ m^2 s^{-1}), the characteristic timescale for salt diffusion $\tau_{diff} = L_c^2/D_s$ could be a few hours depending on the characteristic length scale of the evaporator L_c (the thickness of evaporator t_s for 1D diffusion). When τ_{diff} is on the order of an hour – comparable with the daily operation duration, steady-state ($t \gg \tau_{diff}$) cannot be reached and therefore the time-dependent term in eqn (7) should be considered. In addition, the concentration gradient also induces a density gradient. The liquid density (represented by the green triangle in Fig. 8b) is higher near the liquid–air interface due to the higher salt concentration and long salt diffusion time. For liquid–air interfaces that are perpendicular to the direction of gravity – a common configuration – the concentration-driven density gradient could induce natural convection, potentially accelerating salt migration (Fig. 8b). Therefore, the convection term in eqn (7), coupled with the density gradient induced flow, should also be considered. Convective transport of salt is also affected by temperature-induced changes in liquid density. Due to thermal localization in front-side evaporators, the temperature close to the liquid–air interface is higher than the bulk which induces a density gradient (represented by the red triangle in Fig. 8b) in a direction opposite to that induced by the concentration gradient. The net density gradient (represented by the blue triangle in Fig. 8b) should be a superposition of the concentration and temperature induced gradients, which could either drive or suppress convection depending on its direction. In addition, the transient behavior of convection, including the timescale for developing the convective flow and the dynamic

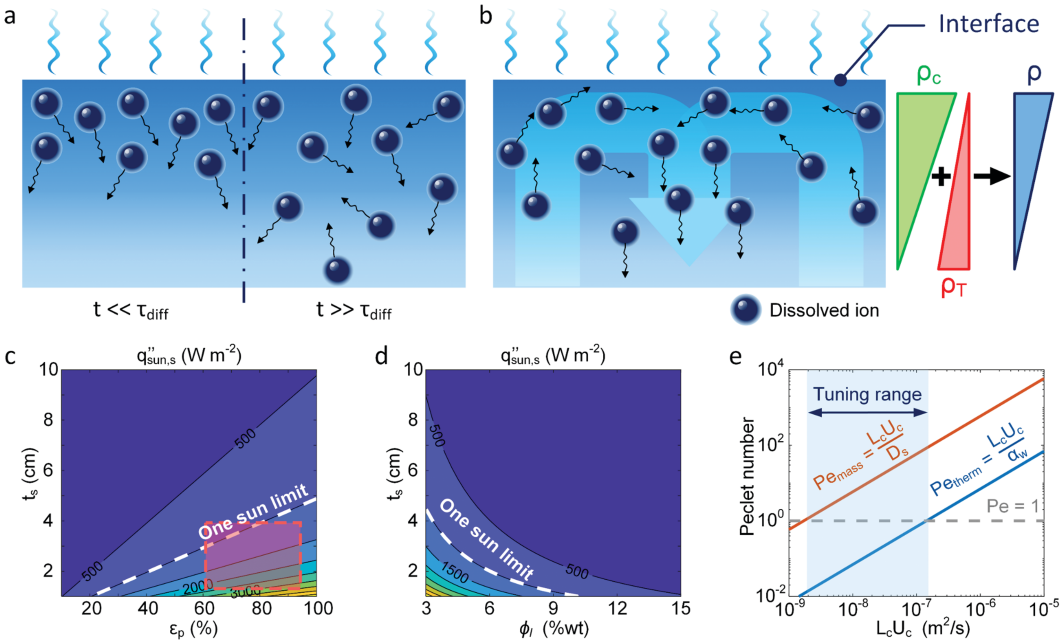

Fig. 8 Salt transport mechanism in thermally-localized solar desalination devices. (a) Schematic representing the transient behavior during salt diffusion. Left side of (a): salt diffusion is a transient process when the operating duration t is comparable or smaller than its characteristic timescale τ_{diff}. Right side of (a): salt diffusion reaches steady state when $t \gg \tau_{diff}$. (b) Schematic showing salt convection due to concentration and temperature induced density gradient. Green triangle: liquid density distribution ρ_c induced by higher salt concentration near the liquid–air interface due to evaporation. Red triangle: liquid density distribution ρ_T induced by higher temperature near the liquid–air interface due to thermal localization. Blue triangle: the cumulative liquid density distribution ρ across the evaporator after combining the concentration (ρ_c) and temperature (ρ_T) induced effects. The density distribution shown in (b) shows a case when ρ can drive convection. However, depending on the relative magnitudes of ρ_c and ρ_T, the gradient of ρ can either trigger or suppress natural convection. (c) Critical solar flux for salt separation $q''_{sun,s}$ as a function of evaporator thickness t_s and porosity ε_p. When the solar flux is larger than $q''_{sun,s}$, salt crystallization occurs at the liquid–air interface. For this calculation, seawater salinity of 3.5 g L^{-1} (3.4 wt%) is assigned to bulk water. The white-dashed line shows the one sun limit, and the red-dashed box indicates the typical operation regime of the evaporator. (d) Critical solar flux for salt separation $q''_{sun,s}$ as a function of evaporator thickness t_s and bulk water concentration ϕ_l. The porosity of the evaporator is assumed to be 80%. The white-dashed line shows the one sun limit. (e) Heat (Pe_{therm}) and mass (Pe_{mass}) transport Peclet numbers as a function of the product of evaporator characteristic length scale L_c and characteristic flow velocity U_c. The blue band in (e) shows a tuning range for the evaporator geometry and flow field which simultaneously ensures $Pe_{mass} > 1$ and $Pe_{therm} < 1$, *i.e.*, convection is the dominant mode for salt rejection while the corresponding total heat loss contribution is negligible.

response due to the change of solar flux, needs to be well-understood to ensure sufficiently fast redistribution of the salt. Therefore, a mechanistic model of salt transport is necessary to quantify the above effects in different operating conditions.

Here, we provide a simplified analysis of salt transport in 1D assuming steady-state diffusion. Fig. 8c shows the critical solar flux for salt separation $q''_{sun,s}$ as a function of evaporator thickness and porosity. The critical solar flux for salt separation is defined as the absorbed solar flux corresponding to saturation salt concentration at the liquid-air interface, beyond which salt crystallization will occur in the evaporator. The salinity of bulk water is assumed to be 35 g L^{-1} (3.4 wt%) – same as that of typical seawater. $q''_{sun,s}$ decreases rapidly with increasing t_s and decreasing ε_p due to the resulting increase in diffusion resistance. The line representing the one sun limit ($q''_{sun,s}$ = 1000 W m^{-2}, white-dashed line in Fig. 8c) crosses the typical operation regime (red-dashed box in Fig. 8c), indicating that salt accumulation is relatively common and can be a severe problem for solar thermal desalination. Salt accumulation can be even more problematic for applications dealing with high-concentration salt water such as wastewater treatment. Fig. 8d shows the critical solar flux for salt separation as a function of evaporator thickness and bulk water concentration ϕ_l, when the evaporator porosity is 80%. $q''_{sun,s}$ decreases with increasing ϕ_l due to a decrease of concentration gradient between the liquid–air interface and bulk water. When $t_s > 1$ cm and $\phi_l > 10$ wt%, it is almost impossible to completely reject salt only relying on diffusion under one sun illumination (the white-dashed line in Fig. 8d).

Since salt rejection through diffusion alone is relatively inefficient, it is desirable to enhance salt transport using natural convection which can be triggered by concentration as well as temperature gradients. It is also possible to introduce forced convection to further accelerate the salt rejection, which can be driven by gravity or additional mechanical parts. However, since convective flow will also increase heat loss, the trade-off between enhancing salt rejection and reducing heat loss needs to be carefully considered. Fig. 8e shows the potential opportunity to accelerate salt rejection by engineering the fluid flow. The contribution of convection relative to diffusion is quantified by the Peclet number. The Peclet

numbers for heat and mass transport are given by $Pe_{therm} = L_c U_c/\alpha_w$ and $Pe_{mass} = L_c U_c/D_s$, respectively, where U_c is the characteristic flow velocity and α_w is the thermal diffusivity of water. When the Peclet number is significantly smaller than one, diffusion is the dominant transport mechanism. When the Peclet number is significantly larger than one, convection becomes more important. Fig. 8e shows Pe_{therm} and Pe_{mass} as a function of $L_c U_c$. For efficient salt rejection *via* convection, it is desirable to have a large enough flow velocity U_c such that $Pe_{mass} > 1$. Meanwhile, U_c should be small enough such that, $Pe_{therm} < 1$, which ensures that the additional heat loss due to convection is negligible. Since α_w ($\sim 10^{-7}$ m^2 s^{-1}) and D_s ($\sim 10^{-9}$ m^2 s^{-1}) typically differ by two orders of magnitude, there exists a tuning range (blue band in Fig. 8e) where $Pe_{mass} > 1$ and $Pe_{therm} < 1$ hold simultaneously – achievable through evaporator geometry and fluid flow engineering. Specific strategies enabling optimization of mass and thermal transport and its impact on the overall salt rejection and water production need to be investigated in future studies.

4.2. Strategies for avoiding salt accumulation and accelerating salt rejection

In this section, we summarize several practical strategies for avoiding salt accumulation and accelerating salt rejection based on a fundamental understanding of salt transport discussed above. In general, these strategies can be classified into four categories, *i.e.*, (1) separation by function, (2) enhanced salt diffusion/convection, (3) water confinement without porous media, and (4) contactless heating. The separation by function strategy focuses on reducing the side effects of salt accumulation.[85,115–118] Xu *et al.* developed a Janus absorber using a double-layer structure, which decouples the solar absorbing and capillary wicking functionalities (top panel of Fig. 9a).[115] The upper layer is hydrophobic, acting as the solar absorber whereas the bottom layer is hydrophilic, creating capillary pressure for water supply. Since salt can only accumulate in the bottom layer, it no longer affects solar absorption. Xia *et al.* demonstrated a spatially isolating strategy to preserve the evaporation area, while salt crystallization is confined to the edge of the circular disk evaporator due to the large transport resistance from the edge to the center (bottom panel of Fig. 9a).[85] Although the separation by function strategy is capable of reducing the side effects of salt accumulation, it cannot enhance salt rejection which is particularly important for desalinating high-concentration salt water. Improved salt rejecting performance can be achieved by engineering diffusion/convection resistance.[70,86,119] Kuang *et al.* created more salt diffusion pathways by drilling vertical channels on a carbonized natural wood evaporator, which shortens the distance between the evaporating interface and bulk water (left panel of Fig. 9b) – demonstrating enhanced salt rejection during a six-hour continuous test using 20 wt% NaCl solution.[119] Ni *et al.* designed similar vertical channels using hydrophilic cellulose fabric, which enables both water transport and salt rejection (right panel of Fig. 9b).[70] More interestingly, in addition to concentration gradient-driven salt diffusion, natural convection was observed in the experiment and confirmed as the major driving force of salt rejection using numerical simulations.[70] Similarly, Morciano *et al.*[68] and Zhang *et al.*[67] also demonstrated enhanced salt rejection by engineering Marangoni and unidirectional flow, respectively. However, to fully take advantage of the enhanced salt diffusion/convection strategy, quantitative optimization of the geometry, number, size, and spacing of salt rejection channels is required.

Since the increase in salt transport resistance due to the porous evaporator is one of the main reasons for salt accumulation, the water confinement approach achieved thermal localization without a porous evaporator.[44,120] Wu *et al.* designed a conical solar evaporator with asymmetric ratchets and microcavity arrays on the surface, which creates a capillary pressure gradient for water confinement and unidirectional water transport (left panel in Fig. 9c).[120] Salt crystallization is localized at the apex of the conical evaporator due to the Marangoni effect, which has negligible effect on the evaporation process. High solar-to-vapor conversion efficiency of 96% was demonstrated in desalinating 25 wt% NaCl solution under one sun illumination.[120] Xu *et al.* developed a waterlily-inspired solar evaporator where water layer is confined between a hydrophobic porous solar absorber and a thermal insulating layer (right panel in Fig. 9c).[44] Heat is localized into this confined water layer due to heat transfer from the absorber and thermal insulation from the bulk water at the bottom. Salt rejection from the confined water layer to the bulk water is achieved through the macroscopic holes in the thermal insulating layer (right panel in Fig. 9c). This design achieved about 80% solar-to-vapor conversion efficiency for a 10 wt% NaCl solution under one sun illumination.[44] The water confinement strategy has inspired a new pathway for the thermally-localized evaporator design, however, its integration with desalination devices requires further investigation.

Contactless heating is another effective approach to avoid fouling due to the complete separation between the absorber and water surface and removal of the evaporator (Fig. 9d), where desalinating 25 wt% NaCl solution has been demonstrated under one sun illumination.[63,64] Although superior anti-fouling performance has been shown, the demonstrated solar-vapor conversion efficiency for the contactless configuration is still relatively low (about 25% for superheated vapor generation[63] and 43% for wastewater treatment[64]), indicating a potential opportunity to significantly improve performance through a better understanding of the heat and mass transport. In addition to the above strategies, salt rejections using ion exchange by adding chemicals,[117,121] directional solvent extraction,[122] selective ion penetration materials,[123] and self-rotating evaporator[124] are also promising for integration with solar desalination devices.

Our discussion in this section mainly focused on NaCl-accumulation induced fouling and reliability. Although

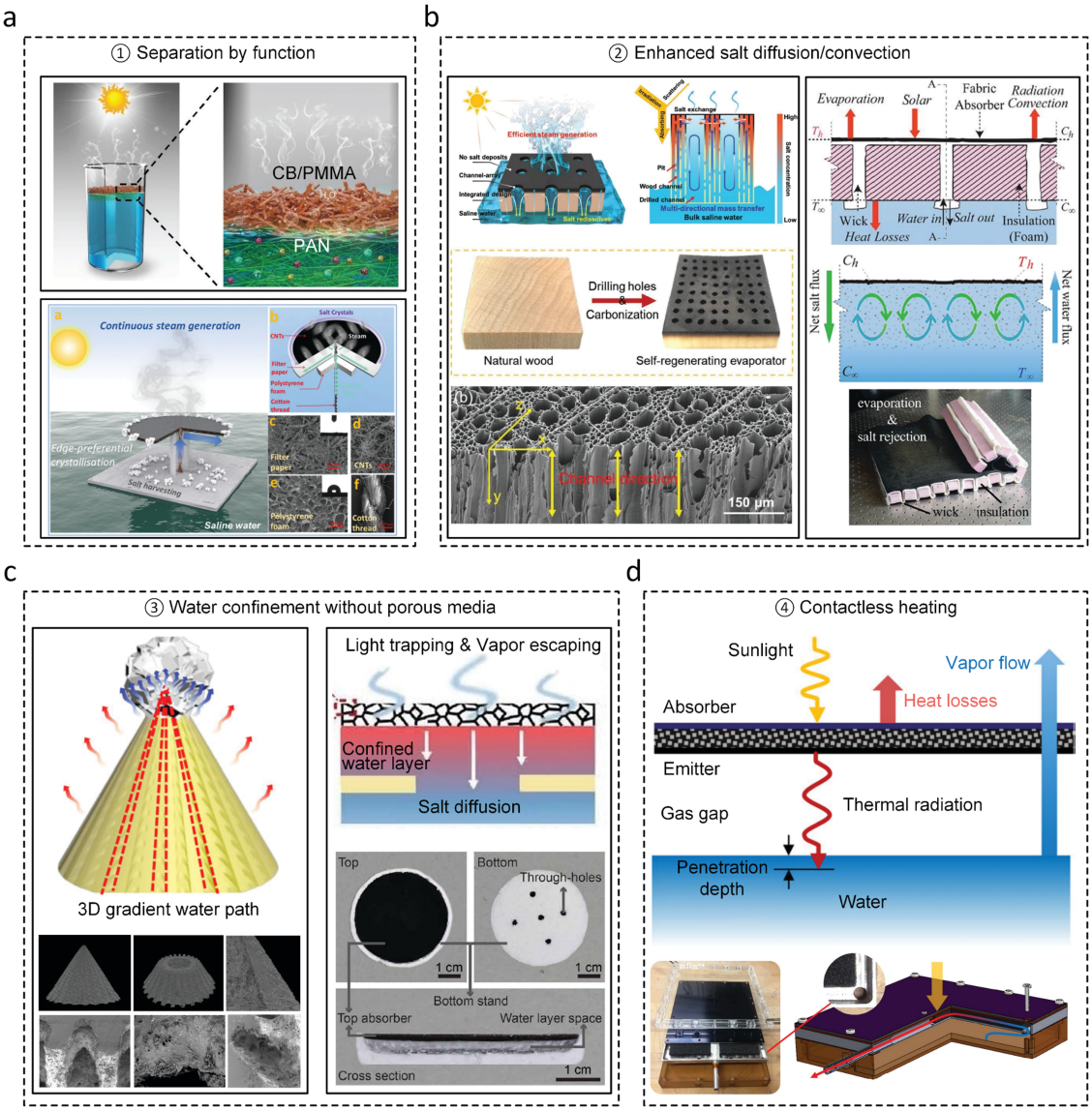

Fig. 9 Strategies for avoiding salt accumulation and accelerating salt rejection. (a) Representative examples of the separation by function strategy[85,115] which focuses on eliminating side-effects due to salt accumulation. Reproduced with permissions from John Wiley and Sons[115] and Royal Society of Chemistry.[85] (b) Representative examples of the enhanced salt diffusion/convection strategy[70,119] which accelerates salt rejection by reducing the salt transport resistance. Reproduced with permissions from John Wiley and Sons[119] and Royal Society of Chemistry.[70] (c) Representative examples of the water confinement strategy[44,120] which removes the porous evaporator that induces salt accumulation and localizes heat in the confined water layer. Reproduced with permissions from Springer Nature[120] and American Association for the Advancement of Science.[44] (d) Representative example of the contactless heating strategy[63] which addresses the fouling and inefficient salt rejection due to the contact between the absorber and water surface. Reproduced with permissions from Springer Nature.[63]

dissolved salt (NaCl) is one of the major species causing fouling and has attracted most attention, other salts like sulfates and carbonates, organic compounds like hydrocarbons, and biological organisms might lead to significant fouling during operation. For example, the crystallization of species with very low solubility in water (*e.g.*, Ca^{2+} and $CaSO_4 \cdot 2H_2O$) can be even more challenging in real practice and typical salt rejection tests using NaCl solution can be inadequate. Therefore, in-depth analysis of other fouling mechanisms, anti-fouling strategies, and long-term robustness tests in realistic environments also need to be performed in future studies.

5. Techno-economic analysis of thermally-localized solar desalination

The primary driving force behind the significant interest in thermally-localized solar desalination in recent years is its potential economic-feasibility and scalability which can enable widespread adoption. In this section, we highlight the interplay between different device designs and efforts to achieve high water production, long-lasting reliability, and low material cost. Using a simple techno-economic analysis, we evaluate the cost competitiveness of desalination devices with varying target production rates and device costs.

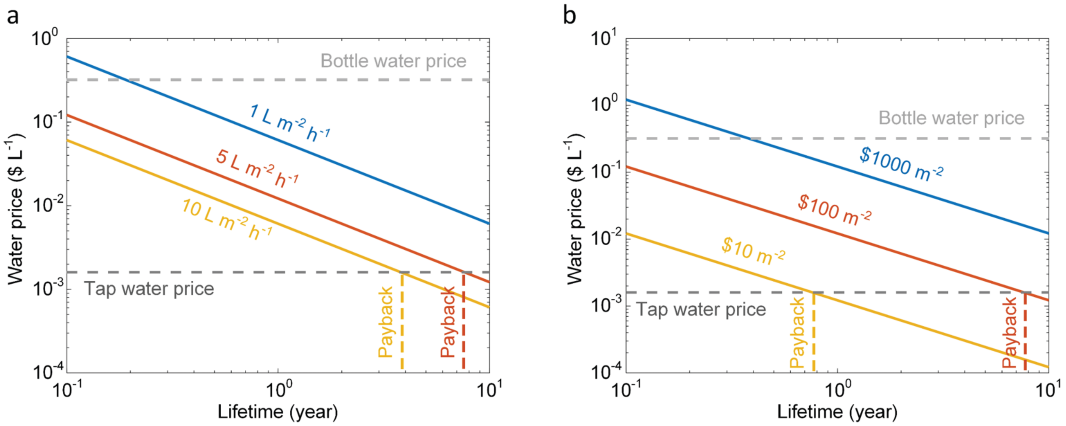

Fig. 10 Techno-economic analysis for thermally-localized solar desalination. (a) Price of desalinated water as a function of device lifetime when the production rate is 1 L m^{-2} h^{-1}, 5 L m^{-2} h^{-1} and 10 L m^{-2} h^{-1}. This analysis used a device cost of \$100 m^{-2}. (b) Price of desalinated water as a function of device lifetime when the device cost is \$1000 m^{-2}, \$100 m^{-2} and \$10 m^{-2}. This analysis used a water production rate of 5 L m^{-2} h^{-1}. The desalinated water price is compared with bottled water price (light-grey dashed line) and tap water price (dark-grey dashed line). The payback period is the required device lifetime when the corresponding desalinated water price is equal to the tap water price (yellow and orange dashed lines).

The aggregate cost of materials, manufacturing, labor, and maintenance represent the total device cost since solar desalination does not consume electricity. The unit price for purified water P_w (units: \$ L^{-1}) is thus given by,[36]

$$P_w = \frac{C_m}{R_w \times I_{irr} \times T_{life}} \quad (8)$$

where C_m is the total device cost per unit area (units: \$ m^{-2}), R_w is the water productivity per unit area (units: L kWh^{-1}), I_{irr} is the average daily solar irradiance (units: kWh m^{-2} day^{-1}) and T_{life} is the device lifetime (units: days). We use I_{irr} = 4.5 kWh m^{-2} day^{-1} – the average daily solar irradiance of the United States in our calculation.[125] Note that solar desalination will become more economically feasible when operated in regions with higher solar irradiance. To be consistent, we use the water production rate under one sun illumination in this analysis, which can be easily converted to R_w based on the incident solar flux. Fig. 10a shows the desalinated water price as a function of device lifetime for different water production rates. The device cost is assumed to be \$100 m^{-2} – already achievable based on current designs.[34,69,70] Increasing the lifetime can significantly reduce the price of produced water, which highlights the importance of improving reliability. Compared with bottled water,[126,127] water produced by thermally-localized solar desalination is generally more cost-effective (the light-grey dashed line in Fig. 10a). However, to make desalinated water economically competitive with tap water,[128] longer lifetimes and higher production rates are required (the dark-grey dashed line in Fig. 10a). The figure also shows the payback period which represents the lifetime when the corresponding desalinated water price is equal to the tap water price (indicated by the yellow and red dashed lines in Fig. 10). When the lifetime of a desalination device is larger than the payback period, it becomes economically feasible. For a device with 1 L m^{-2} h^{-1} production rate (blue line in Fig. 10a) – comparable to the performance of a single stage device – the payback period is estimated to be more than ten years. The payback period can be significantly reduced by improving the production rate. For example, the payback period is about four years when the production rate is 10 L m^{-2} h^{-1} (yellow line in Fig. 10a), which highlights the advantage of multistage devices. Fig. 10b shows that reducing the device cost can significantly lower the water price when the production rate is fixed at 5 L m^{-2} h^{-1}. For example, the payback period can be less than one year if the device cost can be reduced to \$10 m^{-2}. Therefore, to realize a commercially competitive solar desalination device, a water production rate greater than 5 L m^{-2} h^{-1}, device cost less than \$100 m^{-2} and lifetime longer than a few years are desired.

6. Conclusions and perspectives

This review highlights the significant potential of solar desalination in addressing the global water shortage. Specifically, this paper focused on thermally-localized solar desalination systems which can simultaneously achieve flexibility and high energy efficiency. Instead of focusing on the material composition and morphology, we classified the evaporators and desalination devices reported in the literature based on their configurations – front-side and back-side. Although most of the current designs use the front-side configuration, we show that the back-side evaporator is advantageous since it offers greater flexibility in the choice of materials, integration with condenser, and heat loss suppression. Back-side desalination devices are also more desirable because they allow a wide range of materials for condenser, enhance condensation heat transfer, and avoid reduction of incident solar flux due to interfering condensed droplets.

We analyzed different strategies to improve water production and presented a theoretical framework which can be used to quantitatively guide the design for both the evaporator and desalination device. Specifically, we focused on three factors limiting the evaporator performance – heat loss, coupling of

heat and mass transport, and water transport. We show that heat loss and coupling of heat and mass transport are critical in determining solar-vapor conversion efficiency, while the water transport capability is usually not a bottleneck due to the dilute solar flux. Using a theoretical framework, we analyzed the effectiveness of three thermal management strategies employing a spectrally selective absorber, convection cover, and conduction barrier; indicating that improper thermal insulation accounts for more than 75% reduction in solar-vapor conversion efficiency.

An important point that is often overlooked is that the water productivity of a desalination device is largely independent of its evaporator performance in an open system because the heat and mass transfer mechanisms are different. An important design parameter – the air gap thickness between the evaporator and condenser – governs the solar-to-vapor conversion efficiency of the desalination device. An optimal air gap thickness exists due to the transition from a heat transfer limited to a mass transfer limited regime. The insights gained from modeling and experiments indicate that device-level heat and mass transport optimization is as important as advancements in evaporator materials. In addition, we show that the efficient recycling of latent heat using a multistage design is critical to achieving a multifold enhancement in desalination performance, where more than 600% solar-vapor conversion efficiency and about 10 L m^{-2} h^{-1} water production rate are predicted. Quantitative optimization of the number of stages, device size, and air gap thickness is important to approach the theoretical limit. Similar to the single-stage design, an optimal air gap thickness also exists for the multistage desalination device.

In addition to increasing the water production, enhancing reliability is equally important for a high-performance desalination device. We analyzed the salt transport due to diffusion and convection using a theoretical framework and show that salt accumulation can be significant even under natural sunlight due to the low diffusivity of ions in water. We also show the complex salt transport processes due to the coupling of temperature- and concentration-induced fluid flow, which could inform future research opportunities to accelerate salt rejection. In addition, we reviewed different strategies for avoiding salt accumulation and accelerating salt rejection including separation by function, enhanced salt diffusion/convection, water confinement without porous media, and contactless heating.

Finally, in order to evaluate the real-world feasibility of thermally-localized solar desalination, we performed a techno-economic analysis that took into account the efficacy of water production and reliability. Three parameters determine the commercial feasibility of a device – water production rate, lifetime, and device cost. Compared with bottled water, solar desalination is generally more cost-effective. However, to be comparable with the price of tap water, solar desalination is expected to have a water production rate greater than 5 L m^{-2} h^{-1}, device cost less than \$100 m^{-2}, and lifetime longer than a few years.

In summary, this review provides a comprehensive analysis of the recent progress and future opportunities of thermally-localized solar desalination, which could enable its transition from laboratory prototypes to industrial applications. With efforts that increase water production, enhance anti-fouling capability, and reduce device cost, we believe efficient, robust, and thermally-localized solar desalination will become economically feasible and play an important role in addressing the global water crisis.

Conflicts of interest

There are no conflicts to declare.

Acknowledgements

L. Zhang gratefully acknowledges funding support from MIT Martin Family Society of Fellows for Sustainability, Abdul Latif Jameel Water and Food Systems Lab (J-WAFS), and Singapore-MIT Alliance for Research and Technology (SMART) LEES Program. Z. Xu acknowledges funding supports from the National Natural Science Foundation of China (Grant No. 51976123) and Shanghai Pujiang Program (Grant No. 2019PJD022).

References

1 M. M. Mekonnen and A. Y. Hoekstra, *Sci. Adv.*, 2016, **2**, e1500323.
2 M. A. Shannon, P. W. Bohn, M. Elimelech, J. G. Georgiadis, B. J. Mariñas and A. M. Mayes, *Nature*, 2008, **452**, 301–310.
3 R. W. Hofste, S. Kuzma, S. Walker, E. H. Sutanudjaja, M. F. P. Bierkens, M. J. M. Kuijper, M. F. Sanchez, R. V. Beek, Y. Wada, S. G. Rodriguez and P. Reig, Aqueduct 3.0: Updated Decision-Relevant Global Water Risk Indicators, https://www.wri.org/publication/aqueduct-30, (accessed 11 November 2020).
4 M. S. Mauter and P. S. Fiske, *Energy Environ. Sci.*, 2020, **13**, 3180–3184.
5 GDP per capita (current US$), https://data.worldbank.org/indicator/NY.GDP.PCAP.CD?end=2019&start=1960&view=chart, (accessed 11 November 2020).
6 Solar irradiance data, https://solargis.com/, (accessed 11 November 2020).
7 Z. Wang, T. Horseman, A. P. Straub, N. Y. Yip, D. Li, M. Elimelech and S. Lin, *Sci. Adv.*, 2019, **5**, eaax0763.
8 Y. Zhang, T. Xiong, D. K. Nandakumar and S. C. Tan, *Adv. Sci.*, 2020, **7**, 1903478.
9 Y. Pang, J. Zhang, R. Ma, Z. Qu, E. Lee and T. Luo, *ACS Energy Lett.*, 2020, **5**, 437–456.
10 P. Tao, G. Ni, C. Song, W. Shang, J. Wu, J. Zhu, G. Chen and T. Deng, *Nat. Energy*, 2018, **3**, 1031–1041.
11 X. Li, G. Ni, T. Cooper, N. Xu, J. Li, L. Zhou, X. Hu, B. Zhu, P. Yao and J. Zhu, *Joule*, 2019, **3**, 1798–1803.
12 S. K. Patel, S. K. Patel, C. L. Ritt, A. Deshmukh, Z. Wang, M. Qin, M. Qin, R. Epsztein, M. Elimelech and M. Elimelech, *Energy Environ. Sci.*, 2020, **13**, 1694–1710.
13 F. Zhao, Y. Guo, X. Zhou, W. Shi and G. Yu, *Nat. Rev. Mater.*, 2020, **5**, 388–401.

14 X. Zhou, Y. Guo, F. Zhao and G. Yu, *Acc. Chem. Res.*, 2019, **52**, 3244–3253.
15 E. Chiavazzo, M. Morciano, F. Viglino, M. Fasano and P. Asinari, *Nat. Sustain.*, 2018, **1**, 763–772.
16 J. Lienhard, M. Antar, A. Bilton, J. Blanco and G. Zaragoza, *Annu. Rev. Heat Transfer*, 2012, **15**, 267–347.
17 A. E. Kabeel and S. A. El-Agouz, *Desalination*, 2011, **276**, 1–12.
18 A. E. Kabeel, *Energy*, 2009, **34**, 1504–1509.
19 A. El-Bahi and D. Inan, *Renewable Energy*, 1999, **17**, 509–521.
20 P. I. Cooper, *Sol. Energy*, 1973, **15**, 205–217.
21 J. Xiong, G. Xie and H. Zheng, *Energy Convers. Manage.*, 2013, **73**, 176–185.
22 H. Tanaka, T. Nosoko and T. Nagata, *Desalination*, 2000, **130**, 279–293.
23 G. Prakash Narayan, M. G. St. John, S. M. Zubair and J. H. Lienhard, *Int. J. Heat Mass Transfer*, 2013, **58**, 740–748.
24 G. P. Narayan, K. M. Chehayeb, R. K. McGovern, G. P. Thiel, S. M. Zubair and J. H. Lienhard, *Int. J. Heat Mass Transfer*, 2013, **57**, 756–770.
25 M. W. Shahzad, M. Burhan, L. Ang and K. C. Ng, *Desalination*, 2017, **413**, 52–64.
26 H. Ghasemi, G. Ni, A. M. Marconnet, J. Loomis, S. Yerci, N. Miljkovic and G. Chen, *Nat. Commun.*, 2014, **5**, 4449.
27 Z. Wang, Y. Liu, P. Tao, Q. Shen, N. Yi, F. Zhang, Q. Liu, C. Song, D. Zhang, W. Shang and T. Deng, *Small*, 2014, **10**, 3234–3239.
28 G. Ni, G. Li, S. V. Boriskina, H. Li, W. Yang, T. Zhang and G. Chen, *Nat. Energy*, 2016, **1**, 16126.
29 L. Zhou, Y. Tan, J. Wang, W. Xu, Y. Yuan, W. Cai, S. Zhu and J. Zhu, *Nat. Photonics*, 2016, **10**, 393–398.
30 K. Bae, G. Kang, S. K. Cho, W. Park, K. Kim and W. J. Padilla, *Nat. Commun.*, 2015, **6**, 10103.
31 F. Zhao, X. Zhou, Y. Shi, X. Qian, M. Alexander, X. Zhao, S. Mendez, R. Yang, L. Qu and G. Yu, *Nat. Nanotechnol.*, 2018, **13**, 489–495.
32 X. Zhou, F. Zhao, Y. Guo, Y. Zhang and G. Yu, *Energy Environ. Sci.*, 2018, **11**, 1985–1992.
33 Y. Guo, X. Zhao, F. Zhao, Z. Jiao, X. Zhou and G. Yu, *Energy Environ. Sci.*, 2020, **13**, 2087–2095.
34 Z. Xu, L. Zhang, L. Zhao, B. Li, B. Bhatia, C. Wang, K. L. Wilke, Y. Song, O. Labban, J. H. Lienhard, R. Wang and E. N. Wang, *Energy Environ. Sci.*, 2020, **13**, 830–839.
35 W. Wang, Y. Shi, C. Zhang, S. Hong, L. Shi, J. Chang, R. Li, Y. Jin, C. Ong, S. Zhuo and P. Wang, *Nat. Commun.*, 2019, **10**, 3012.
36 L. Zhang, Z. Xu, B. Bhatia, B. Li, L. Zhao and E. N. Wang, *Appl. Energy*, 2020, **266**, 114864.
37 L. Zhu, M. Gao, C. K. N. Peh and G. W. Ho, *Nano Energy*, 2019, **57**, 507–518.
38 V.-D. Dao, N. H. Vu and S. Yun, *Nano Energy*, 2020, **68**, 104324.
39 P. Wang, *Environ. Sci.: Nano*, 2018, **5**, 1078–1089.
40 H. Liu, Z. Huang, K. Liu, X. Hu and J. Zhou, *Adv. Energy Mater.*, 2019, **9**, 1900310.
41 C. Zhang, H. Liang, Z. Xu and Z. Wang, *Adv. Sci.*, 2019, **6**, 1900883.
42 M. Gao, L. Zhu, C. K. Peh and G. W. Ho, *Energy Environ. Sci.*, 2019, **12**, 841–864.
43 C. Chen, Y. Kuang and L. Hu, *Joule*, 2019, **3**, 683–718.
44 N. Xu, J. Li, Y. Wang, C. Fang, X. Li, Y. Wang, L. Zhou, B. Zhu, Z. Wu, S. Zhu and J. Zhu, *Sci. Adv.*, 2019, **5**, eaaw7013.
45 J. Yang, Y. Pang, W. Huang, S. K. Shaw, J. Schiffbauer, M. A. Pillers, X. Mu, S. Luo, T. Zhang, Y. Huang, G. Li, S. Ptasinska, M. Lieberman and T. Luo, *ACS Nano*, 2017, **11**, 5510–5518.
46 X. Li, W. Xu, M. Tang, L. Zhou, B. Zhu, S. Zhu and J. Zhu, *Proc. Natl. Acad. Sci. U. S. A.*, 2016, **113**, 13953–13958.
47 F. Jiang, H. Liu, Y. Li, Y. Kuang, X. Xu, C. Chen, H. Huang, C. Jia, X. Zhao, E. Hitz, Y. Zhou, R. Yang, L. Cui and L. Hu, *ACS Appl. Mater. Interfaces*, 2018, **10**, 1104–1112.
48 Y. Ito, Y. Tanabe, J. Han, T. Fujita, K. Tanigaki and M. Chen, *Adv. Mater.*, 2015, **27**, 4302–4307.
49 C. Jia, Y. Li, Z. Yang, G. Chen, Y. Yao, F. Jiang, Y. Kuang, G. Pastel, H. Xie, B. Yang, S. Das and L. Hu, *Joule*, 2017, **1**, 588–599.
50 P. Mu, Z. Zhang, W. Bai, J. He, H. Sun, Z. Zhu, W. Liang and A. Li, *Adv. Energy Mater.*, 2019, **9**, 1802158.
51 X. Hu, W. Xu, L. Zhou, Y. Tan, Y. Wang, S. Zhu and J. Zhu, *Adv. Mater.*, 2017, **29**, 1604031.
52 P. Zhang, J. Li, L. Lv, Y. Zhao and L. Qu, *ACS Nano*, 2017, **11**, 5087–5093.
53 H. Liu, X. Zhang, Z. Hong, Z. Pu, Q. Yao, J. Shi, G. Yang, B. Mi, B. Yang, X. Liu, H. Jiang and X. Hu, *Nano Energy*, 2017, **42**, 115–121.
54 Q. Ma, P. Yin, M. Zhao, Z. Luo, Y. Huang, Q. He, Y. Yu, Z. Liu, Z. Hu, B. Chen and H. Zhang, *Adv. Mater.*, 2019, **31**, 1808249.
55 L. Zhou, Y. Tan, D. Ji, B. Zhu, P. Zhang, J. Xu, Q. Gan, Z. Yu and J. Zhu, *Sci. Adv.*, 2016, **2**, e1501227.
56 O. Neumann, A. S. Urban, J. Day, S. Lal, P. Nordlander and N. J. Halas, *ACS Nano*, 2013, **7**, 42–49.
57 G. Ni, N. Miljkovic, H. Ghasemi, X. Huang, S. V. Boriskina, C.-T. Lin, J. Wang, Y. Xu, M. M. Rahman, T. Zhang and G. Chen, *Nano Energy*, 2015, **17**, 290–301.
58 L. Zhang, B. Tang, J. Wu, R. Li and P. Wang, *Adv. Mater.*, 2015, **27**, 4889–4894.
59 X. Zhou, F. Zhao, Y. Guo, B. Rosenberger and G. Yu, *Sci. Adv.*, 2019, **5**, 1–8.
60 J. Li, X. Wang, Z. Lin, N. Xu, X. Li, J. Liang, W. Zhao, R. Lin, B. Zhu, G. Liu, L. Zhou, S. Zhu and J. Zhu, *Joule*, 2020, **4**, 928–937.
61 X. Li, J. Li, J. Lu, N. Xu, C. Chen, X. Min, B. Zhu, H. Li, L. Zhou, S. Zhu, T. Zhang and J. Zhu, *Joule*, 2018, **2**, 1331–1338.
62 Y. Shi, R. Li, Y. Jin, S. Zhuo, L. Shi, J. Chang, S. Hong, K.-C. Ng and P. Wang, *Joule*, 2018, **2**, 1171–1186.
63 T. A. Cooper, S. H. Zandavi, G. W. Ni, Y. Tsurimaki, Y. Huang, S. V. Boriskina and G. Chen, *Nat. Commun.*, 2018, **9**, 5086.

64 A. K. Menon, I. Haechler, S. Kaur, S. Lubner and R. S. Prasher, *Nat. Sustain.*, 2020, **3**, 144–151.
65 G. Xue, Q. Chen, S. Lin, J. Duan, P. Yang, K. Liu, J. Li and J. Zhou, *Glob. Challenges*, 2018, **2**, 1800001.
66 X. Wang, Y. Liu, R. Feng, Y. Zhang, C. Chang, B. Fu, T. Luan, P. Tao, W. Shang, J. Wu, C. Song and T. Deng, *Prog. Nat. Sci.: Mater. Int.*, 2019, **29**, 10–15.
67 Y. Zhang, H. Zhang, T. Xiong, H. Qu, J. J. Koh, D. K. Nandakumar, J. Wang and S. C. Tan, *Energy Environ. Sci.*, 2020, **13**, 4891–4902.
68 M. Morciano, M. Fasano, S. V. Boriskina, E. Chiavazzo and P. Asinari, *Energy Environ. Sci.*, 2020, **13**, 3646–3655.
69 Z. Liu, H. Song, D. Ji, C. Li, A. Cheney, Y. Liu, N. Zhang, X. Zeng, B. Chen, J. Gao, Y. Li, X. Liu, D. Aga, S. Jiang, Z. Yu and Q. Gan, *Glob. Challenges*, 2017, **1**, 1600003.
70 G. Ni, S. H. Zandavi, S. M. Javid, S. V. Boriskina, T. A. Cooper and G. Chen, *Energy Environ. Sci.*, 2018, **11**, 1510–1519.
71 Y. Liu, S. Yu, R. Feng, A. Bernard, Y. Liu, Y. Zhang, H. Duan, W. Shang, P. Tao, C. Song and T. Deng, *Adv. Mater.*, 2015, **27**, 2768–2774.
72 A. F. Mills, *Heat Transfer*, Pearson Education, 1999.
73 G. Vaartstra, L. Zhang, Z. Lu, C. D. Díaz-Marín, J. C. Grossman and E. N. Wang, *J. Appl. Phys.*, 2020, **128**, 130901.
74 L. Zhang, L. Zhao and E. N. Wang, *Int. Commun. Heat Mass Transfer*, 2020, **110**, 104255.
75 Z. Lu, I. Kinefuchi, K. L. Wilke, G. Vaartstra and E. N. Wang, *Nat. Commun.*, 2019, **10**, 2368.
76 L. Zhang, Y. Zhu, Z. Lu, L. Zhao, K. R. Bagnall, S. R. Rao and E. N. Wang, *Appl. Phys. Lett.*, 2018, **113**, 163701.
77 A. LaPotin, Y. Zhong, L. Zhang, L. Zhao, A. Leroy, H. Kim, S. R. Rao and E. N. Wang, *Joule*, 2021, **5**, 166–182.
78 L. Zhao, B. Bhatia, S. Yang, E. Strobach, L. A. Weinstein, T. A. Cooper, G. Chen and E. N. Wang, *ACS Nano*, 2019, **13**, 7508–7516.
79 L. Zhao, E. Strobach, B. Bhatia, S. Yang, A. Leroy, L. Zhang and E. N. Wang, *Opt. Express*, 2019, **27**, A39.
80 H. Liu, C. Chen, G. Chen, Y. Kuang, X. Zhao, J. Song, C. Jia, X. Xu, E. Hitz, H. Xie, S. Wang, F. Jiang, T. Li, Y. Li, A. Gong, R. Yang, S. Das and L. Hu, *Adv. Energy Mater.*, 2018, **8**, 1701616.
81 L. A. Weinstein, J. Loomis, B. Bhatia, D. M. Bierman, E. N. Wang and G. Chen, *Chem. Rev.*, 2015, **115**, 12797–12838.
82 L. Zhao, B. Bhatia, L. Zhang, E. Strobach, A. Leroy, M. K. Yadav, S. Yang, T. A. Cooper, L. A. Weinstein, A. Modi, S. B. Kedare, G. Chen and E. N. Wang, *Joule*, 2020, **4**, 1–13.
83 S. C. Singh, M. ElKabbash, Z. Li, X. Li, B. Regmi, M. Madsen, S. A. Jalil, Z. Zhan, J. Zhang and C. Guo, *Nat. Sustain.*, 2020, **3**, 938–946.
84 X. Li, X. Min, J. Li, N. Xu, P. Zhu, B. Zhu, S. Zhu and J. Zhu, *Joule*, 2018, **2**, 2477–2484.
85 Y. Xia, Q. Hou, H. Jubaer, Y. Li, Y. Kang, S. Yuan, H. Liu, M. W. Woo, L. Zhang, L. Gao, H. Wang and X. Zhang, *Energy Environ. Sci.*, 2019, **12**, 1840–1847.
86 S. He, C. Chen, Y. Kuang, R. Mi, Y. Liu, Y. Pei, W. Kong, W. Gan, H. Xie, E. Hitz, C. Jia, X. Chen, A. Gong, J. Liao, J. Li, Z. J. Ren, B. Yang, S. Das and L. Hu, *Energy Environ. Sci.*, 2019, **12**, 1558–1567.
87 Q.-F. Guan, Z.-M. Han, Z.-C. Ling, H.-B. Yang and S.-H. Yu, *Nano Lett.*, 2020, **20**, 5699–5704.
88 Y. Huang, C. Feng, J. Hoeniges, K. Zhu and L. Pilon, *J. Quant. Spectrosc. Radiat. Transfer*, 2020, **251**, 107039.
89 J. W. Rose and L. R. Glicksman, *Int. J. Heat Mass Transfer*, 1973, **16**, 411–425.
90 S. Kim and K. J. Kim, *J. Heat Transfer*, 2011, **133**, 1–8.
91 L. Zhang, Z. Xu, Z. Lu, J. Du and E. N. Wang, *Appl. Phys. Lett.*, 2019, **114**, 163701.
92 R. Tadmor, *Soft Matter*, 2011, **7**, 1577–1580.
93 S. Goh, J. Zhang, Y. Liu and A. G. Fane, *Desalination*, 2013, **323**, 39–47.
94 N. Miljkovic, R. Enright, Y. Nam, K. Lopez, N. Dou, J. Sack and E. N. Wang, *Nano Lett.*, 2013, **13**, 179–187.
95 R. Enright, N. Miljkovic, N. Dou, Y. Nam and E. N. Wang, *J. Heat Transfer*, 2013, **135**, 091304.
96 Z. Xu, L. Zhang, K. Wilke and E. N. Wang, *Langmuir*, 2018, **34**, 9085–9095.
97 L. Zhang, J. Zhu, K. L. Wilke, Z. Xu, L. Zhao, Z. Lu, L. L. Goddard and E. N. Wang, *ACS Nano*, 2019, **13**, 1953–1960.
98 K.-H. Chu, R. Xiao and E. N. Wang, *Nat. Mater.*, 2010, **9**, 413–417.
99 T. ''Leo'' Liu and C.-J. ''CJ'' Kim, *Science*, 2014, **346**, 1096–1100.
100 K.-C. Park, P. Kim, A. Grinthal, N. He, D. Fox, J. C. Weaver and J. Aizenberg, *Nature*, 2016, **531**, 78–82.
101 Y. Hou, Y. Shang, M. Yu, C. Feng, H. Yu and S. Yao, *ACS Nano*, 2018, **12**, 11022–11030.
102 H. Chen, T. Ran, Y. Gan, J. Zhou, Y. Zhang, L. Zhang, D. Zhang and L. Jiang, *Nat. Mater.*, 2018, **17**, 935–942.
103 L. Huang, H. Jiang, Y. Wang, Z. Ouyang, W. Wang, B. Yang, H. Liu and X. Hu, *Desalination*, 2020, **477**, 114260.
104 D. Ghim, X. Wu, M. Suazo and Y.-S. Jun, *Nano Energy*, 2020, 105444.
105 H. T. El-Dessouky, H. M. Ettouney and Y. Al-Roumi, *Chem. Eng. J.*, 1999, **73**, 173–190.
106 H. El-Dessouky, H. I. Shaban and H. Al-Ramadan, *Desalination*, 1995, **103**, 271–287.
107 H. T. El-Dessouky, H. M. Ettouney and F. Mandani, *Appl. Therm. Eng.*, 2000, **20**, 1679–1706.
108 M. Rosso, A. Beltramini, M. Mazzotti and M. Morbidelli, *Desalination*, 1997, **108**, 365–374.
109 H. Tanaka, T. Nosoko and T. Nagata, *Desalination*, 2002, **150**, 131–144.
110 A. D. Khawaji, I. K. Kutubkhanah and J.-M. Wie, *Desalination*, 2008, **221**, 47–69.
111 R. B. Bird, W. E. Stewart and E. N. Lightfoot, *Transport Phenomena*, Wiley, 1960.
112 H. Kim, S. Yang, S. R. Rao, S. Narayanan, E. A. Kapustin, H. Furukawa, A. S. Umans, O. M. Yaghi and E. N. Wang, *Science*, 2017, **356**, 430–434.

113 S. Narayanan, H. Kim, A. Umans, S. Yang, X. Li, S. N. Schiffres, S. R. Rao, I. S. McKay, C. A. Rios Perez, C. H. Hidrovo and E. N. Wang, *Appl. Energy*, 2017, **189**, 31–43.
114 S. Narayanan, S. Yang, H. Kim and E. N. Wang, *Int. J. Heat Mass Transfer*, 2014, **77**, 288–300.
115 W. Xu, X. Hu, S. Zhuang, Y. Wang, X. Li, L. Zhou, S. Zhu and J. Zhu, *Adv. Energy Mater.*, 2018, **8**, 1702884.
116 Y. Yang, H. Zhao, Z. Yin, J. Zhao, X. Yin, N. Li, D. Yin, Y. Li, B. Lei, Y. Du and W. Que, *Mater. Horiz.*, 2018, **5**, 1143–1150.
117 J. Zeng, Q. Wang, Y. Shi, P. Liu and R. Chen, *Adv. Energy Mater.*, 2019, **9**, 1900552.
118 Z. Liu, B. Wu, B. Zhu, Z. Chen, M. Zhu and X. Liu, *Adv. Funct. Mater.*, 2019, **29**, 1905485.
119 Y. Kuang, C. Chen, S. He, E. M. Hitz, Y. Wang, W. Gan, R. Mi and L. Hu, *Adv. Mater.*, 2019, **31**, 1900498.
120 L. Wu, Z. Dong, Z. Cai, T. Ganapathy, N. X. Fang, C. Li, C. Yu, Y. Zhang and Y. Song, *Nat. Commun.*, 2020, **11**, 521.
121 C. Zhang, Y. Shi, L. Shi, H. Li, R. Li, S. Hong, S. Zhuo, T. Zhang and P. Wang, *Nat. Commun.*, 2021, **12**, 998.
122 J. Guo, Z. D. Tucker, Y. Wang, B. L. Ashfeld and T. Luo, *Nat. Commun.*, 2021, **12**, 437.
123 H. Geng, Q. Xu, M. Wu, H. Ma, P. Zhang, T. Gao, L. Qu, T. Ma and C. Li, *Nat. Commun.*, 2019, **10**, 1512.
124 Y. Xia, Y. Li, S. Yuan, Y. Kang, M. Jian, Q. Hou, L. Gao, H. Wang and X. Zhang, *J. Mater. Chem. A*, 2020, **8**, 16212–16217.
125 U.S. Annual Solar GHI, https://www.nrel.gov/gis/solar.html, (accessed 11 November 2020).
126 Tap Water *vs.* Bottled Water, https://www.foodandwaterwatch.org/about/live-healthy/tap-water-vs-bottled-water, (accessed 11 November 2020).
127 A. Livingston, Bottled Water vs. Tap Water – Facts & 4 Reasons to Drink Tap, https://www.moneycrashers.com/bottled-water-vs-tap-water-facts/#:~:text = According to the IBWA%2C, the Environmental Protection Agency (EPA), (accessed 11 November 2020).
128 Average monthly residential cost of water in the U.S. from 2010 to 2019 (in U.S. dollars), https://www.statista.com/statistics/720418/average-monthly-cost-of-water-in-the-us/, (accessed 11 November 2020).